Chapter 3

Vibroelectronic Properties of Functionalized Single-Walled Carbon Nanotubes and Double-walled Boron Nitride Nanotubes

Metin Aydin and Daniel L. Akins

Additional information is available at the end of the chapter

http://dx.doi.org/10.5772/51486

1. Introduction

Carbon is the first element in group-IVof the periodic table and has a $1s^2 2s^2 2p^2$ electronic configuration, in which four valence electrons allow it to form a number of so-called hybridized atomic orbitals. Carbon atoms in elemental substances bond to each other covalently by the sharing of electron pairs, in which the covalent bonds have directional properties; this in turn provides carbon the capability to form various molecular and crystalline solid structures. The nature of the covalent bonds that are formed dictate the varied chemical and physical properties of carbon allotropes. Pure carbon-based materials not only exist as the commonly recognizeddiamond and graphite allotropes, but also more exotic entities such as fullerenes, carbon nanotubes (CNTs), and graphene; these latter allotropes having proven themselves important materials in nanotechnology.

The present chapter deals with single-walled carbon nanotubes (SWNTs), whose unique properties, as suggested above, derive from their distinctive structure. In SWNTs the carbon bonding that exists is akin to that that exists in graphite as opposed to that found in diamond. More specifically, diamond has a coordination number of four, with sp^3 hybridization, while, on the other hand, sp^2 hybridization exists in the planar layers of carbon atoms that give graphite its structure, and in the bonding that leads to the tubular structure of SWNTs. The sp^2 hybridization in graphite links carbon atoms in a two-dimensional (2D) layer of hexagons that lead to each layer in the graphite structure, in the ideal case, forming a planar structure. Each carbon atom contributes 3 electrons to 3 equivalent sigma bonds within the plane and has 1 electron left in the perpendicular p_z orbitals; such electrons are delocalized over the entire plane, resulting in a π-electron orbital system that allows the

fourth valence electron to essentiallymove freely over the plane. Within the layers, the carbon-carbon bond distance is similar to the bond length in benzene (i.e., the carbon atoms are strongly bound to each other and the carbon-carbon distance is about 0.14 nm), leading to a very large inplane value for Young's modulus. However, the distance between layers (ca., 0.34 nm) is sufficiently large that the layers are bounded to each other mainly by weak, long-range Van der Waals type interaction. The weak interlayer coupling gives graphite the property of a seemingly very soft material, a property that makes graphite suitable for use in pencils and in lubricants.

As a result of its intrinsic structure, the electrical conductivity of graphite is directionally-dependent. Delocalized π-electrons parallel to the planes essentially experience metallic conduction, while electron mobility perpendicular to the layered planes would typically be much lower, but with possibly significant temperature dependency, thereby imbruing graphite as semiconductor character as well. The directionality of the conductivity translates to a band structure that has a filled valence bandand an empty conduction band separated by an energy gap. These bands, in one picture, would result from bonding and antibonding molecular π-orbitals that can be conceptualized in terms of energy lowering and energy raising combination of the perpendicular p_z atomic orbitals. The π-bonding orbitals would be fully occupied while the π-antibonding orbitals would be unoccupied, with the gap being the energy difference between the top and bottom of the respective orbitals. Because of the larger distance between its layers, graphite may form intercalation compounds with added species that act as electron donors, with graphite acting as an electron acceptor, incorporating the donated electrons into the vacant conduction band; or as electron acceptors, where graphite donates electrons from the full valence band. In diamond, it is to be noted that all valence electrons are localized around the carbon atoms, hence, such a structural characteristic has profound effectson its electrical properties, with diamond being an insulator with a band gap around 6 eV.

We now move to a more focused discussion of carbon nanotubes. Carbon nanotubes (CNTs) were discovery in 1991 [1], their unique physical, chemical, and electronic properties have led to a variety of technological application in functional nanodevices, especially as transistors and sensors [2, 3, 4], [5, 6, 7], in heat conduction systems [8, 9], in specialty electronics [10, 11], molecular memories [12], optics [13, 14, 15], electrically excited single-molecule light sources [16, 17, 18, 19], to functionalized DNA [20, 21], high-performance adsorbent electrode material for energy-storage device [22], and protein functionalization [23, 24].

As it is well known, carbon nanotubes can be obtained by rolling up a defined projected area from within the hexagonal lattice of a graphene sheet in a seamless fashion such that all carbon–carbon (C–C) valences are satisfied, and the direction in which the roll up is performed transforms into the circumference of the tube. The projected area is in fact a homomorphic representation of a particular carbon nanotube [48(f-g)]. The roll-up vector is also termed the chiral vector, and is defined as $n\vec{a}_1 + m\vec{a}_2$, where $\vec{a}_1$ and $\vec{a}_2$ are the unit vectors of the hexagonal lattice, and n and m are the so-called chiral indices. An infinite number of nanotube geometries are possible, with a specific nanotube characterized by chiral indices (n,m), which, in turn, define the chiral angle θ and tube diameter (d_t); the latter is also de-

http://dx.doi.org/10.5772/51486

pendent on the C–C bond length of the hexagonal lattice. For n = m, the nanotube is said to have the "armchair" conformation; for $n \neq 0$ and m = 0, the conformation is called "zigzag"; while for $n \neq 0$ and $m \neq 0$ the conformation is termed "chiral."The diameter of the nanotube normally has values that range up to several nanometers from ~0.4 nm, while nanotubes are usually several microns in length. It is to be noted that single-walled and multi-walled carbon nanotubes generally have properties that are significantly different, while double-walled carbon nanotubes (DWNTs) can be viewed as representing the key structure that defines the transition between SWNTs and MWNTs.

Carbon nanotubes can be metallic or semiconducting depending on their structure. This is due to the symmetry and the unique electronic structure of graphene. If the chiral indices are equal, n = m, the nanotube is metallic; if n−m is a multiple of 3, then the nanotube is semiconducting, with a very small band gap; otherwise, the nanotube is a moderate semiconductor [25]. Interestingly, some nanotubes have conductivities higher than that of copper, while others behave more like silicon.

As it is well known, the optical properties of nanotubes are implicitly connected with the absorption, photoluminescence, and Raman spectroscopy of nanotubes. Such optical measurements permit a reliable characterization of the quality of nanotube, such as chirality, size, and structural defect. In the case of Raman measurements, even though a large number of phonon modes of carbon nanotubes would be expected, most of them are Raman inactive due to the selection rules that emanate from the high symmetry properties of the nanotubes. The Raman spectrum of a carbon nanotube exhibits a few characteristic modes that can be used to determine the size of nanotubes and to classify the type of the nanotubes, such as semiconducting and metallic. For example, in the low frequency region, one type of characteristic vibration is called the radial breathing mode (RBM); this movement of the carbon atoms is in the radial direction with the same phase, and corresponds to vibration of the entire tube, which is strongly diameter dependent [48(f-g)]. The RBM gives precise information about the nanotube diameter and is typically found between 100 cm^{-1} and 500 cm^{-1}. Additionally, in the high energy range from (1000 to 2000 cm^{-1}), there are two important characteristic Raman bands: the defect induced disordered band (D-band) that appears between 1300 and 1400 cm^{-1}, and tangential modes (G-band) that lie in the range from ~1560 to ~1600 cm^{-1}. The D-band is present in all graphite-like carbons and originates from structural defects. Therefore, the intensity ratio of the G/D modes is conventionally used to quantify the structural quality of carbon nanotubes. The G-band corresponds to planar vibrations of carbon atoms and is present in most graphite-like materials (at around 1580 cm^{-1}). This tangential mode (G-band) in SWCNT is split into several peaks. The splitting pattern and intensity depend on the tube structure and excitation energy; they can be used, though with much lower accuracy compared to RBM mode, to estimate the tube diameter and whether the tube is metallic or semiconducting. [48(f-g)].

Chemical functionalization by bond formation or by coating the nanotubes with organic/inorganic molecules or by encapsulating a varieties of semiconductor particles, including CdSe and CdTe, may lead to efficient energy transfer between the molecules and nanotube, as well as lead to significant enhancement in the optical properties of the composite [26, 27, 28, 29]. As an example of effect on an optical property, it has been reported that when a squarylium dye isencapsulated into a carbon nanotube, increased chemical and thermal stability of squaryli-

um molecules occur, which, since encapsulation of a dye quenches strong dye luminescence, allows measurement and analysis of the dye's Raman spectra[30]. Also, L. Alvarez *et al.*[31] have reported that while infrared spectroscopy (IR) might provide evidence of a significant positive charge transfer for an inserted oligothiophene, Raman spectra evince different behaviors depending on the excitation energy and relationship to the oligomer's (specifically, quaterthiophene) optical absorption energy. For example, at high excitation wavelength (far from the oligomer's resonance), radial breathing modes exhibit a significant blue-shift as a result of the encapsulation effect, while at low excitation wavelength, close to resonance with the oligomer absorption, both the G-band and the low-frequency modes vanish, suggesting a significant charge transfer between the oligomer and the nanotube.

CNTs are also widely used in the clinical and research medical arenas. They find application as superior drug delivery media, for health monitoring devices; as biosensing platforms for the treatment of various diseases; in chemical sensor devices, etc. [32, 33, 34, 35]. Functionalized-SWNTs (i.e., f-SWNTs) have been known to increase solubility and permit efficient tumor targeting/drug delivery; prevents SWNTs from being cytotoxic; and possibly altering the functioning of immune cells. Moreover, carbon nanotubes have enhanced solubility when functionalized with lipids that make their movement through the human body easier and reduces the risk of blockage of vital body organ pathways. Also, CNTs exhibit strong optical absorbance in certain spectral windows, such as the NIR (near-infrared); when functionalized within tumor cell with specific binding entities, the nanotubes have allowed the selective destruction of disease (e.g., cancer) cells with NIR in drug delivery applications.

More recently, boron nitride nanotubes (BNNTs) can be counted among the modified CNT that have been synthesized [36, 37, 38]. The electronic properties of boron nitride nanotubes differ from carbon nanotubes: while carbon nanotubes can be either metallic or semiconducting, depending on their chirality and radius [39], all boron nitride nanotubes (BNNTs) are found to be semiconducting materials with a large band gap[40]. And since the band gap is large, the gap energy is only weakly dependent on the diameter, chirality, and the number of walls of a multi-walled tube structure. Moreover, because of their semiconducting character, BNNTs like CNTs themselves are also very interesting materials for application in nanoscale devices, and have been considered alternatives to CNTs [41, 42]. Like CNTs the modification of the electronic properties of BNNTs by doping and functionalization is an important avenue for making nanodevices. The doped BNNTs nanotubes may exhibit a dramatic change relative to the pristine nanotube. Furthermore, because of the strong interactions between electrons and holes in BNNTs [43, 44], the excitonic effects in BNNTs have proven more important than in CNTs. Bright and dark excitons in BNNTs qualitatively alter the optical response [45].

For a better understanding of the physical and optical properties of nanotubes, quantum mechanical calculations have been extremely helpful. In this chapter, we provide theoretical results on double-walled boron nitride nanotubes (DWBNNTs) and functionalized nanotubes using DFT; this report extends the quantum chemical computational approach that we have used earlier [48(f-g)]. The results of calculations not only indicate the shift in the spectral peak positions of the RBM and G-modes in Raman spectra of DWBNNTs relative to

http://dx.doi.org/10.5772/51486

their corresponding isolated SWBNNTs, but also indicatesa charge transfer from the outer-shell to the inner-shell when DWBNNTs are excited, as discussed in Section 3. Furthermore, the plots of the frequencies of vibrational radial breathing modes (RBM) versus $1/d_t$ for (2n, 0)&(n,0)-DWBNNTs exhibit a strong diameter dependence.

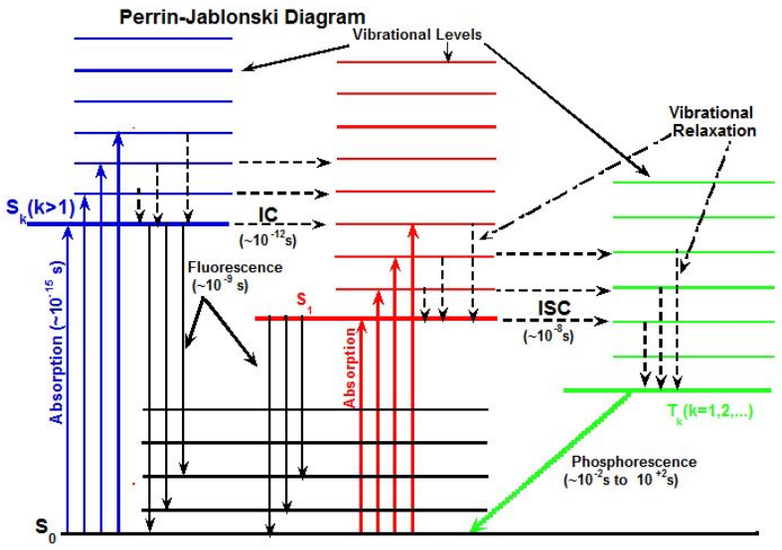

Figure 1. A general Perrin-Jablonski diagram for a fluorescent molecule, where S and T stand for singlet and triplet electronic states, respectively. IC and ISC represent "internal conversion" and "intersystem crossing", respectively.

For functionalized single-walled carbon nanotubes, we find that there should be a charge transfer process directed from the nanotube to an attached molecule, which is active in optical excitations. More generally, upon irradiation a system can undergo internal conversion (IC) and intersystem crossing (ISC) processes, in addition to photochemical and other photophysical processes. Transient intermediates are likely to form in the IC and ISC radiationless processes, herein referred to as "dark processes," which are not detected using conventional light absorption or emission spectroscopic methods. As seen from the combined Perrin-Jablonski diagram in Figure 1, for a typical molecule the emission of a photon from an electronically excited state to the ground state results in fluorescence in the region of 300 to 1500 nm. Photophysical processes for an isolated molecule occur as a result of transitions between the different internal energy states of that comprise the electronic states. A molecular system in the gas-phase or in the solution phase at room temperature is mostly expected to be in its ground state (S_0). The excitation of a molecular system from its ground state to an excited vibroelectronic state by absorption of a photon (occurring within ca. 10^{-15} second) is much faster than a emission of the photon from its excited electronic state (S_k, k>1) to its ground state (occurring in ca. 10^{-8} second). All of the excited molecular systems may not directly return back to their ground state by emission of a photon, $S_{k>0} \rightarrow S_0$ transition, but some of them may return back to their ground states (S_0) by internal conversion (CI), for instance, when the molecule is excited into a higher vibroelectronic state (S_k>1), it may undergo relaxation to the S_1 state (in 10^{-12} s) via vibrational coupling between these states before

undergoing additional vibrational relaxation and returning to the lowest singlet electronic energy level (S_1), referred to as internal conversion. Subsequently, transition from S_1 to S_0 by emission of a photon (fluorescence) occurs. An alternate pathway for a molecule in the lowest energy S_1 state involves intersystem crossing (at rates that can compete with fluorescence) by the molecule into a triplet state T_1. From T_1, the molecule can undergo radiative de-excitation via a much slower process, which is known as phosphorescence ($T_1 \rightarrow S_0$ transition), such as illustrated by the Perrin-Jablonski diagram given in Figure 1.

It is to be noted that fluorescence resonance energy transfer (FRET) can be used to investigate intra- and/or intersystem energy transfer dynamics that might occur as one transitions fromsingle-walled nanotubes (SWNTs) to multi-walled nanotubes (MWNTs),or to the functionalized nanotubes (f-NTs). Such dark intermediates are expected to play crucial roles in IC and ISC processes and thus are fundamental to understanding mechanistic photochemistry of the functionalized-nanotubes and multi-walled nanotubes. We have used time-dependent DFT (i.e., TD-DFT) methods to determine the dark transient structures involved in radiationless processes for functionalized-SWCNTs and DWBNNTs. Also, we have calculated all possible singlet-triplet vertical electronic transitions and discussed these in terms of IC and ISC processes.

It is to be noted that CNTs have been shown to exhibit strong optical absorbances in certain spectral windows, such as the NIR (near-infrared). Moreover, when functionalized with tumor cell specific binding entities CNTs have facilitated the selective destruction of disease cells (e.g., cancer cell) in the NIR and play a significant role in drug delivery applications[46]. In the present chapter, we acknowledge the importance of calculating the IR spectra of both functionalized-SWCNTs and DWBNTS.

2. Results and discussion

Computational methods: The ground state geometries of single-walled carbon nanotubes (SWCNTs), double-walled carbon nanotubes (DWCNTs), single-walled boron nitride nanotubes (SWBNNTs), and functionalized-SWCNTs were optimized without symmetry restriction on the initial structures. Both structure optimization and vibrational analysis calculations were implemented using DFT with functionals, specifically, B3LYP, in which the exchange functional is of Becke's three parameter type, including gradient correction, and the correlation correction involves the gradient-corrected functional of Lee, Yang and Parr. The basis set of split valence type 6-31G, as contained in the Gaussian 03 software package[47], was used. The results of the calculations did not produce any imaginary frequencies. The vibrational mode descriptions were made on the basis of calculated nuclear displacements using visual inspection of the animated normal modes (using GaussView03) [47], to assess which bond and angle motions dominate the mode dynamics for the nanotube. The DFT method was chosen because it is computationally less demanding than other approaches as regards inclusion of electron correlation. Moreover, in addition to its excellent accuracy and favorable computation expense ratio, the B3LYP calculation of Raman fre-

quencies has shown its efficacy in numerous earlier studies performed in this laboratory and by other researchers, often proving itself the most reliable and preferable method for many molecular species of intermediate size, including anions and cations [48]. In our calculations, hydrogen atoms have been placed at the end points of the unit cells. Furthermore, the time-dependent density functional theory at TD-B3LYP level were applied to calculate the vertical electronic transitions for the SWCNTs, SWBNNTs and functionalized (7,0)- and (10,0)-SWCNTs. For geometry optimization and calculations of electronic transitions, the 6-31G* basis set was used for sulfur atom (S) and the 6-31G basis set was used for the other atoms involved in the covalently functionalized nanotubes. It is worth nothing that the results of the calculated structural and spectroscopic properties of the double-walled boron nitride nanotubes (DWBNNTs) and the functionalized zigzag single-walled carbon nanotubes (f-(n, 0)-SWCNTs) used in this chapter have been submitted to elsewhere for publication.

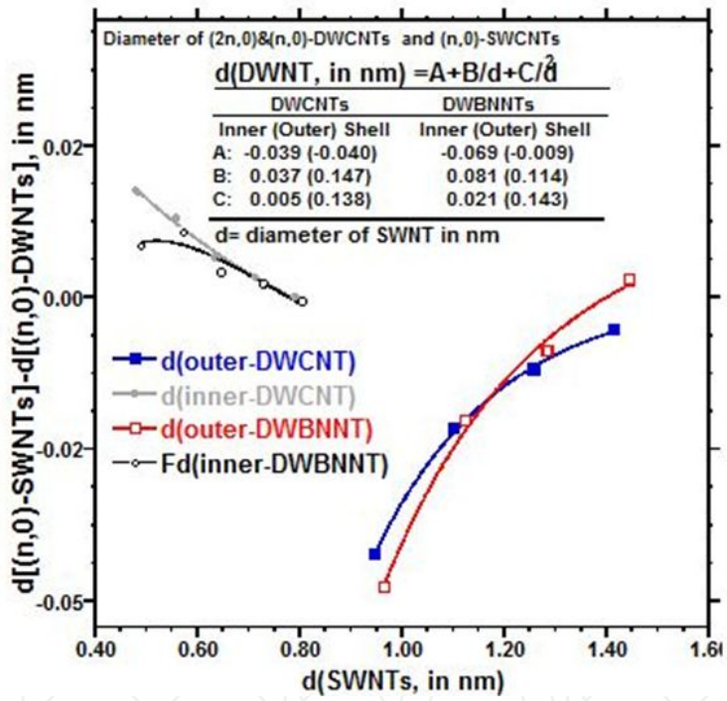

Figure 2. Calculated diameters of the double-walled carbon nanotubes, (2n,0)&(n,0)-DWCNTs, and double-walled boron nitride nanotubes, (2n,0)&(n,0)-DWBNNTs, for n = 6 to 10

3. Results and discussion

3.1. Structural results

Calculated diameters of the (0,n)&(0,2n)-DWCNTs (zigzag double-walled carbon nanotube) and (0,n)&(0,2n)-DWBNNTs (zigzag double-walled boron nitride nanotubes), for n = 6 to 10, were found to decrease for the inner-nanotube and increase for the outer-nanotube, referenced to the corresponding diameter of the zigzag single-wall nanotube ((0,n)-SWNT) which

changes with n. A fit to the calculated individual tube diameters for each inner- and outer-shell of the DWCNTs and DWBNNTs using a functional form that depends inversely on single-walled nanotube's diameter: fit parameters are shown in Eq. 1a-2b

$$\begin{aligned} D_t\left(\text{outer}-\text{shell}-\text{DWCNT}\right),\ \text{in nm}) &= -0.040+\frac{0.147}{d_t}+\frac{0.138}{d_t^2} \quad a \\ D_t\left(\text{inner}-\text{shell}-\text{DWCNT}\right),\ \text{in nm}) &= -0.039+\frac{0.037}{d_t}+\frac{0.005}{d_t^2} \quad b \end{aligned} \tag{1}$$

$$\begin{aligned} D_t\left(\text{outer}-\text{shell}-\text{DWBNNT}\right),\ \text{in nm}) &= -0.009+\frac{0.114}{d_t}+\frac{0.143}{d_t^2} \quad a \\ D_t\left(\text{inner}-\text{shell}-\text{DWBNNT}\right),\ \text{in nm}) &= -0.069+\frac{0.081}{d_t}+\frac{0.021}{d_t^2} \quad b \end{aligned} \tag{2}$$

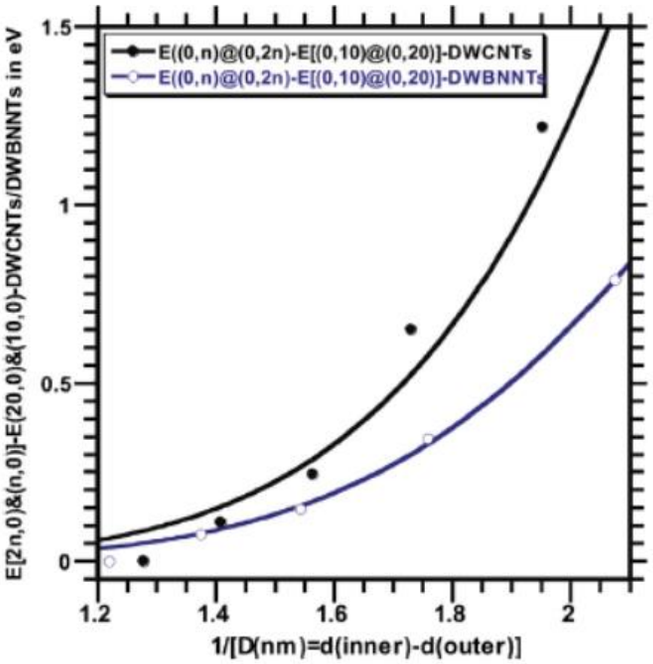

Figure 3. The diameter dependence of the curvature energies of the DWCNTs and DWBNNTs referenced to the global energies per hexagon of the (0,10)&(0,20)-DWCNTs/DWBNNTs is well fitted by a Lennard–Jones potential expression as given in Eqs. (3a) and (3b).

A comparison the diameters of the inner- and outer-shells of the DWNTs with their corresponding SWNTs diameters show that the inner-shells diameters decrease and the outer-shells diameters increased. These predictions explicitly indicate the existence of intertube interactions in DWCNT systems. As seen in Figure 3, the diameter dependence of the curvature energies of the DWCNTs and DWBNNTs referenced to the global energies per hexagon

http://dx.doi.org/10.5772/51486

of the (0,10)&(0,20)-DWCNTs and -DWBNNTs is well fitted by a Lennard-Jones potential expression ($E_{LJ} = -\left(\frac{A}{r^6} - \frac{B}{r^{12}}\right)$ where parameters of the are A and B are van der Waals interaction parameters in Lennard-Jones potential) as given in equation 3a-b,

$$\Delta E\left(\text{DWBNNTs, in eV}\right) = -\left(\frac{0.503}{D_t(\text{nm})}\right)^6 \left\{1 - \left(\frac{0.266(\text{nm})}{D_t(\text{nm})}\right)^6\right\} \quad a$$
$$\Delta E\left(\text{DWCNTs, in eV}\right) = -\left(\frac{0.477}{D_t(\text{nm})}\right)^6 \left\{1 - \left(\frac{0.356(\text{nm})}{D_t(\text{nm})}\right)^6\right\} \quad b \qquad (3)$$

where $\Delta E\left(\frac{\text{DWCNTs}}{\text{DWBNNTs}}\right) = E[(2n, 0)\,\&\,(n, 0)] - E[(20,0)\,\&\,(10,0)]$ and $D_t = d_o(\text{outer shell}) - d_i(\text{inner shell})$ $D_t = d_t(\textit{outer shell}) - d_t(\textit{inner shell})$. The results of the calculations suggest that the DWNTs with large diameters can be much more easily formed than those with small diameters. When comparing the formation energy of the DWCNTs with the DWBNNTs, as shown in Figure 3, it can be seen that the formation of the DWBNNTs is favorable to that of DWCNTs due to the relatively strong interactions between the inner- and outer-shells in the case of the DWBNNTs. This finding also is supported by the calculated electron density, as discussed below, as well as the relative change in the tube diameters when going from the SWNT to the DWNT, as seen in equations 1-2. Furthermore, our ongoing calculations on the energetically stability of the DWBNNTs as function of the interwall distance (between inner- and outer-shells) indicates that the interwall distance around 0.34 nm is more stable, which are excellent agreement with the experimental observations by J. Cumings [59], which will be published elsewhere. However, at different experimental conditions, the DWBNNTs with small interwall distance such as (0,6)&(0,12)-DWBNNT might be formed at different experimentally conditions. The DWBNNTs with small interwall distance might be more interesting than other, in their optical applications.

Figures 4 A-B illustrate the calculated electron density of (12,0)&(6,0)-DWCNT and (0,n)&(0,2n)-DWBNNT, n= 6 and 8. For (12,0)&(6,0)-DWCNT, the geometry optimization, without any symmetry restriction, predicted ground state geometry has C_{2v} point group and the electronic state of ground state has singlet-A_1 symmetry. The plotted electron density showed that while first four highest occupied molecular orbitals (from HOMO to HOMO-4, of B_2, B_1 and $2E_2$ symmetries, respectively) involve both the inner- and outer-shell, the HOMO-5 with the $2E_1$ symmetry belongs to outer-shell only. The lowest unoccupied molecular orbital, LUMO (E_1) lies about 4.699 eV above the HOMO (B_2), and belongs to the inner-shell, while the next higher one (E_1) involves not only the inner- and outer-shell (lies 5.521 eV above the HOMO (A_1)), but also there is a significant sigma-bonding interaction between the inner and outer tubes in the excited state. For the (0,6)&(0,12)-DWCNT, the calculated electron density of (0,6)&(0,12)-DWCNT shows that the first four highest occupied molecular orbitals (from HOMO to HOMO-3, with the A_{1u}, A_{2g} and $2E_{1g}$ symmetries, respectively) belong to the outer-shell and the next higher occupied molecular orbitals, from HOMO-4 to HO-

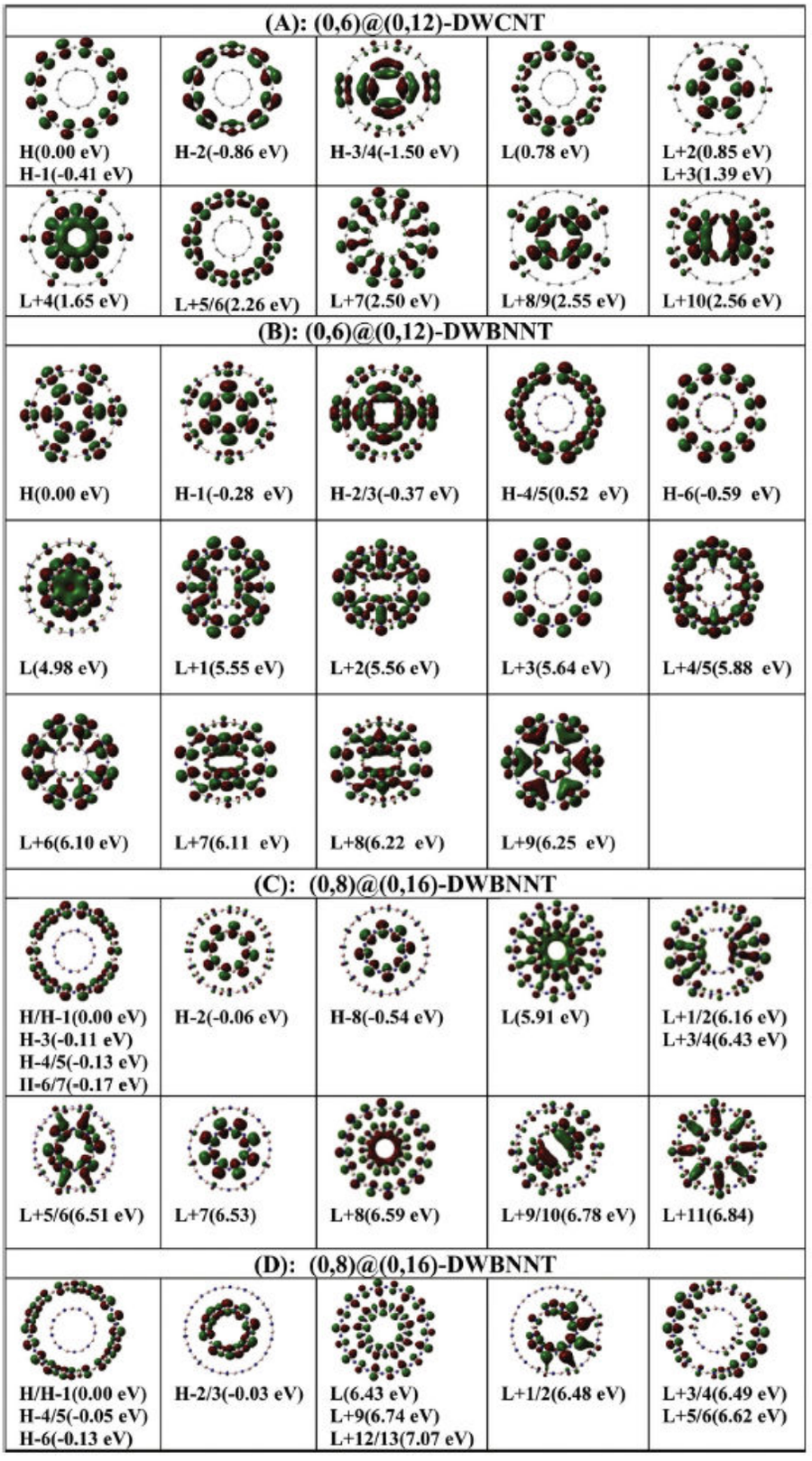

Figure 4. Calculated electron densities in the HOMO and LUMO states: A for the (0,6)&(0,12)-DWCNT, B for (0,6)&(0,12)-DWBNNT, C for (0,8)&(0,16)-DWBNNT, and D for (0,9)&(0,18)-DWBNNT.

MO-24, include both inner- and outer-shells of (0,6)&(0,12)-DWCNT. The lowest unoccupied molecular orbital, LUMO(E_{1u}) lies about 0.780 eV above the HOMO(A_{1u}) and belongs to the outer-shell, while the next one (with B_{2u} symmetry) belongs to the inner-shell, and lies 0.849 eV above the HOMO(A_{1u}). The calculated electron densities also indicate that an intratube (inner and outer tube) interaction may take place in the excited state, since the LUMO +7(A_{2u}), LUMO+8(E_{1u}), LUMO+10(E_{1g}) and LUMO+15(E_{1g}) lie about 2.494, 2.557, 2.563, 3.637 eV above the HOMO(A_{1u}), respectively.

The intratube σ-bonding interaction in the excited state of the (0,6)&(0,12)-DWBNNTs and DWCNT might lead to a probable intertube charge transfer, which can be observed by a significant change in the tangential modes (TMs) of resonance Raman spectra when the tube excited to its intratube charge transfer state. The TMs may not only provide information about the metallic or semiconducting character of nanotubes, but also about the inner-outer tube (intratube) charge transfer. Indeed, very recently, resonant Raman measurements [49], photoemission measurements, and theoretical calculations have provided evidence of charge transfer between the inner- and outer-shells of DWCNTs.

Given such a scenario, small sized-DWCNTs and DWBNNTs might be used as energy conversion systems due to charge transfer between intershells, which might be indicated by changes in of the Raman band intensities upon excitation in resonance with charge transfer between inner- and outer-shells.

3.2. Raman Spectra of Single-Walled and Double-Walled Boron Nitride Nanotube

We calculated Raman spectra for the zigzag single-walled boron nitride nanotube ((0,n)-SWBNNTs, n=6 to 19) and double-walled boron nitride nanotube, (n,0)&(2n,0)-DWBNNTs with n=6 to 9. While the Figs. 5A and 6 provide the calculated Raman spectra for the SWBNNTs and DWBNNTs, respectively, the Figure 7 provides the Raman spectra of the (0,8)&(0,16)-DWBNNT and isolated (0,8)- and (0,16)-SWBNNTs for the comparison. Furthermore, we provided the vibrational mode assignments and frequencies for the DWBNNT and isolated SWBNNTs in Tables 1. All assignments to motions of atoms or groups of atoms in Tables 1 have been accomplished through use of vibration visualization software (specifically, GaussView03). The results of the calculations are summarized below.

Zigzag-SWBNNTs: In the low frequency region (<500 cm^{-1}), the calculated Raman spectra the (0,n)-SWBNNTs (n=6 to 19) exhibited two Raman bands. One of them is known as the radial-breathing mode (RBM) and other is elliptical deformation mode (EDM). The RBM is an important mode for the characterization and identification of particular nanotubes, especially of their chiralities. The importance of the radial-breathing mode for the characterization of nanotubes derives from the inverse dependence of its frequency on the diameter of the nanotube. As seen in Figs. 5A-B, the radial breathing mode (RBM with A_{1g} symmetry, $\omega_{RBM}(A_{1g})$) and other Raman band (elliptical deformation mode (EDM) with E_{2g} symmetry, $\omega_{EDM}(E_{2g})$) have frequencies that inversely depend on a nanotube's diameter. A linear fit to the calculate RBM frequency dependence on nanotube diameter is provided; a linear equation, $\omega_{RBM}(A_{1g}) = 48.51 + \frac{183.54\ cm^{-1}.nm}{d_t(nm)}$, which is in excellent agreement with the results of

the DFT within ± 1 cm^{-1}. However, the offset constant in the linear fitting equation (48.51 cm^{-1}) produce significant error for the (0,n)-SWBNNTs with large diameter because the RBM decreases with increasing tube diameter and RBM in the limit of infinite diameter yields to a simple translation of the BN sheet. The RBM frequency should therefore go to zero in this limit. Therefore, a curve fit may be obtained using a cubic equation such as $\omega_{RBM}(cm^{-1}) = \frac{307.36\ cm^{-1}.nm}{d_t(nm)} - \frac{97.87\ cm^{-1}.nm^2}{[d_t(nm)]^2} + \frac{24.12\ cm^{-1}.nm^3}{[d_t(nm)]^3}$, which reproduces the RBMs within a ± 3 cm^{-1} error range when, comparing with the calculated Raman spectra of the SWBNNTs from (0,6) to (0,19) using the DFT technique and the RBM goes to zero in the limit of infinite diameter. An analytical expression for the other accompanying calculated low frequency bands (EDM of E_{2g} symmetry), which has lower frequency than the RBM, the best fit parameters carried out to third order in inverse diameter parameter is given by the equation: $\omega_{EDM}(E_{2g}) = 113.64 + \frac{29.03\ cm^{-1}.nm}{d_t(nm)} - \frac{14.62\ cm^{-1}.nm^2}{[d_t(nm)]^2} + \frac{6.33\ cm^{-1}.nm^3}{[d_t(nm)]^3}$, which reproduces exact calculated values of the EDMs. It is noting worth that, without offset constant, fitting equation (linear or high order) reproduces the calculated values of the EDMs within a large error range. The band is labeled as EDM for elliptical deformation, which derives from the predominate motions that define vibrational mode motions, as ascertained with the vibration visualization software mentioned earlier.

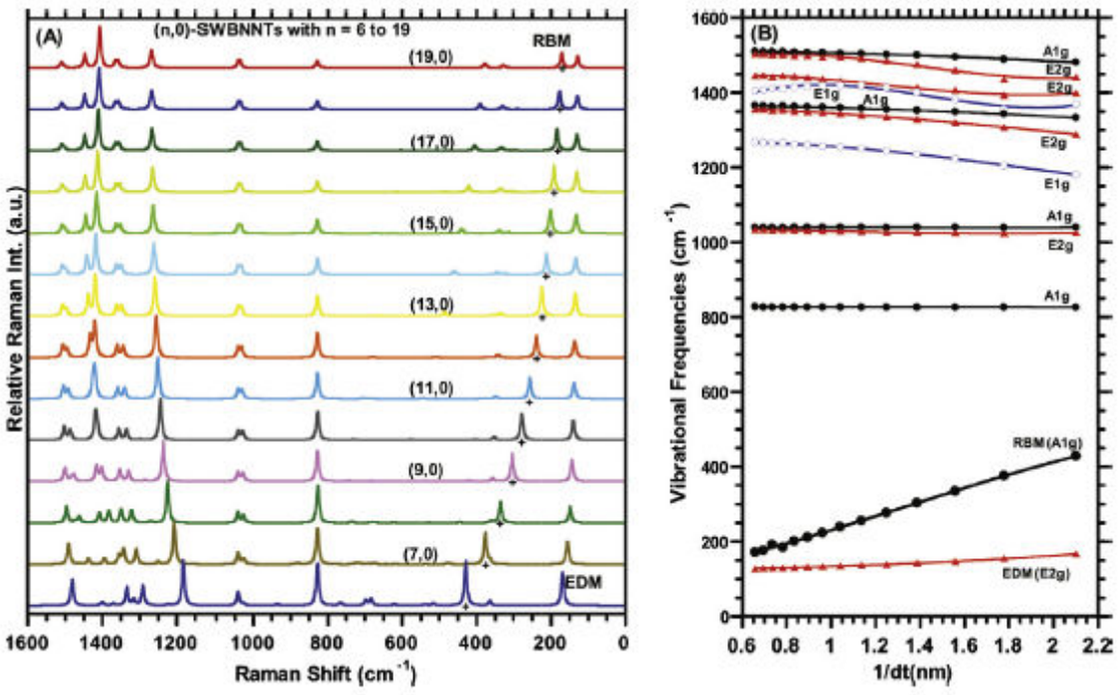

Figure 5. (A) calculated Raman spectra of the (0,n)-SWBNNTs, n = 6–19; (B) the plots of the frequencies of vibrational modes of symmetries A1g, E1g and E2g versus $1/d_t$.

The results of calculated Raman spectra of the (0,n)-SWBNNTs showed that: 1) the RBM of the frequency dramatically increases with decreasing the SWBNNTs diameter, which is not

http://dx.doi.org/10.5772/51486

so surprising since the N–B–N bond strain and the sp^3 hybridization rapidly increases with decreasing SWBNNTs diameter; 2) as seen in Figure 5, for large sized SWBNNTs, the $\omega_{RBM}(A_{1g})$ and $\omega_{EDM}(E_{2g})$ mode frequencies converge. For instance, the calculated frequency separation between the RBM and EDM is found to be 3, 7, 21 and 43 cm^{-1}, when n has the values 26, 25, 22 and 19, respectively. Thus, one can anticipate the (0, 28)-SWBNNT would have unresolvable RBM and EDM bands for the experimental spectra. We can anticipate that the acquisition of Raman spectra for experimental samples consisting of large diameter SWBNNT with the purpose of characterizing the sample in terms of electronic properties and purity may be complicated by the existence of this EDM band, which, in general, can lead to apparent broadening of bands as well as the presence of additional bands that may lead to the erroneous conclusion that more than one type of SWBNNT is present in the sample. Of course, this issue is not expected to be of great significance since the synthesis routes that are presently in vogue do not lead to nanotubes with diameter as large as that corresponding to the (0,26) index. It is to be noted that the E_{2g} band has lower frequencies than the RBM, (see Figure 5A). This latter band is labeled as EDM for elliptical deformation, which derives from the predominate motions that define vibrational mode motions, as ascertained with the vibration visualization software mentioned earlier.

As regards other general conclusions that can be drawn from our calculations for the SWBNNTs, we have found that calculated Raman bands in the mid-frequency region exit nearly size-independent peak positions. As shown in Table 1 or Figs. 5A-B, in the high frequency region there are a few Raman bands of symmetries $E_{1g}/E_{2g}/A_{1g}$ that lie close to one another in frequency. For instance, the calculated Raman modes with symmetries of the A_{1g} (~1355 ± 10 cm^{-1}) and E_{2g} (~1330 ±25 cm^{-1}) approach one another in frequency with increasing diameter of the SWBNNT and then reach a constant values of 1365 and 1356 cm^{-1}, respectively, as seen in Table 1. A fitting equation indicated that these two Raman bands (with symmetries A_{1g} at ~ 1355 ±10 cm^{-1} and E_{2g} (~1330 ±25 cm^{-1}) first increase in frequency then approach a constant value of ~1366 and ~1360 cm^{-1}, respectively, with increasing diameter of the (0,n)-SWBNNT, n=25. Furthermore, the resonance Raman experiments [60,61] have been shown that there is only one strong band at 1355 ± 10 cm^{-1} in high energy region for the boron nitride nanotubes. Thus, the calculated these Raman bands at A_{1g} (~1355 ± 10 cm^{-1}) and E_{2g} (~1330 ±25 cm^{-1}) are not only in good agreement with experiments, but also the calculations suggest that only the Raman band(s) (of the symmetry of A_{1g} and/or E_{2g}) are theatrically enhanced by resonance excitation of the boron nitride nanotube.

Furthermore, the predicted shifts in the peak positions may result from the nanotube curvature effect as mentioned in Refs. 48(f-h), the curvature energy of the nanotube brings about dissimilar force constants along the nanotube axis and the circumference direction. Therefore, the nanotube geometry causes a force constant reduction along the tube axis compared to that in the circumferential direction. Consequently, the curvature effect might play crucial role in the shift of the peak positions of the G-band as well as the RBM band, as mentioned earlier. In addition, the calculated Raman band positions for bands at ~ 1240 ± 30 cm^{-1} are found to be slightly size dependent, exhibiting a slightly blue shift with increasing diameter of the SWBNNTs. This disorder induced mode is also important for the characterization and

	(0,6)	(0,7)	(0,8)	(0,9)	(0,10)	(0,11)	(0,12)	(0,13)	(0,14)	(0,15)	(0,16)	(0,17)	(0,18)	(0,19)	(0,6)& (0,12)	(0,7)& (0,14)	(0,8)& (0,16)	(0,9)& (0,18)
E_{2g}	167	155	147	143	139	137	135	134	133	131	130	130	129	128	246 156	206 147	170 139	152 130
	Elliptical deformation (EDM) of both inner and outer tubes in the same phase																	
A_{1g}	428	376	335	303	277	256	239	224	212	201	192	184	177	171	497 256	416 226	354 200	310 179
	Radial breathing of the outer tube only (RBM)																	
A_{1g}	826	827	826	827	827	827	827	827	827	827	827	827	827	828	820 831	823 832	823 833	823 832
	Out-of-surface bending deformation of the NBN/BNB bonds on the tube																	
E_{2g}	1026	1024	1025	1026	1027	1029	1030	1031	1032	1033	1033	1034	1034	1035	1030	1027	1030	1034
	BN stretching (in opposite phase) along tube axis																	
A_{1g}	1040	1039	1040	1040	1039	1040	1040	1040	1040	1040	1039	1039	1039	1039	1040	1034	1036 1036	1039 1044
	BN stretching along tube axis only																	
E_{2g}	1181	1206	1223	1236	1244	1251	1255	1258	1261	1263	1265	1266	1267	1268	1253 1234	1206 1242	1243 1246	1238 1263
	Asymmetric stretching vibrations and bending deformations of the BNB/NBN bonds																	
E_{1g}	1289	1308	1320	1329	1335	1340	1344	1347	1349	1351	1353	1354	1356	1356		1351	1341	1352
	Bending deformation of the NBN/BNB bonds, including relatively weak BN bond stretching																	
A_{1g}	1333	1343	1349	1353	1355	1358	1360	1361	1362	1363	1363	1364	1364	1365	1371	1368	1358	1363
	BN stretching and bending deformation of the NBN/BNB bonds along tube axis																	
E_{1g}	1370	1355	1382	1401	1413	1419	1419	1418	1416	1414	1412	1410	1408	1406	1366	1398	1373	1376
	Asymmetric stretching vibrations and bending deformations of the BNB/NBN bonds.																	
E_{2g}	1399	1393	1407	1414	1417	1424	1432	1437	1441	1444	1443	1446	1447	1446			1420	1429
	BN stretching and bending deformations of NBN/BNB bonds																	
E1g E2g	1442	1436	1461	1476	1486	1492	1495	1495	1499	1499	1501	1502	1503	1504	1413	1432	1434	1434
	BN stretching, including bending deformations of NBN/BNB bonds																	
A_{1g}	1481	1490	1496	1500	1502	1504	1505	1507	1507	1508	1509	1509	1509	1510	1430 1511	1463 1517	1473 1517	1485 1519
	BN stretching along tube axis, including bending deformations of NBN/BNB bonds																	

Table 1. DFT-calculated Raman vibrational frequencies (in cm^{-1}) and assignments for (0,n)-SWBNNT and (0,n)&(0,2n)-DWBNNTs at the B3LYP/6-31G level.

the defect on the nanotube as observed a broad feature around in the spectrum of the Al-modified MWBNNTs [63]. For example, in the resonance Raman enhanced spectrum, the relative intensity of the disorder mode increases relative to the intensity of the breathing and tangential modes since there is a defect on the nanotube surface as a result of chemical functionalization or caused by structural deformation. For the carbon nanotubes (CNTs), the experimental studies have showed that the increase in the intensity ratio ($I_D/I_{G)}$ indicates an increase in the number of defects on the sidewall of the nanotube. This is expected result of the introduction of covalently bound moieties to the nanotube framework, in which significant amount of the sp^2 carbons is converted to sp^3 hybridization.

DWBNNTs: While Figure 6 provides the calculated nonresonance Raman spectra for the (0,n)&(0,2n)-DWBNNTs, with n ranging from 6 to 9; Figure 8 provides diagrams of the atomic motions associated with the vibrational frequencies for the (8,0)&(16,0)-DWBNNT used as a representative case. The calculations show that the frequencies of the radial breathing modes (RBMs) and tangential modes (TMs, known as G-mode) of (n,0)&(2n,0)-DWBNNT (with n=6 to 9) significantly differ from those calculated for the (0,n)-SWBNNTs (see Figure 7 and Table 1). The results of the calculations are summarized below. In the low frequency region, the calculated Raman spectra of these DWBNNTs exhibited two RBM modes resulting from the radial motion of the inner- and outer-shells, as shown in Figure 6, and both of these RBM modes are strongly diameter dependent. A large gap between RBMs in the Raman spectra of the DWBNNTs decreases with increasing diameter of the inner- and outer-shells (as seen in Figure 6). Comparing these calculated RBMs in the spectrum of the (0,8)&(0,16)-DWBNNT with their corresponding bands in the isolated (0,8)- and (0,16)-SWBNNTs spectra, as seen in Figure 7, we note that the RBMs at 335 cm^{-1} in the Raman spectrum of the (8,0)-SWBNNT and at 192 cm^{-1} in the (16,0)-SWBNNT spectrum are, respectively, upward shifted to 354 and 200 cm^{-1} in the spectrum of (0,8)&(0,16)-DWBNNT. Additionally, the RBMs for the (0,6)-SWBNNT(428 cm^{-1}) and for the (0,12)-SWBNNT (239 cm^{-1}) spectrum are, respectively, blue shifted to 497 and 256 cm^{-1} in the Raman spectrum of (0,6)&(0,12)-DWBNNT (see Table 1). The relative distances between RBMs in the spectra of (0,n)&(0,2n)-DWCNTs are greater than the separation between corresponding RBMs in Raman spectra of (0,n)- and (0,2n)-SWCNTs. For instance, the distance between the RBMs for (0,8)&(0,16)-DWBNNT is 154 cm^{-1}, this distance between the RBMs in the Raman spectra of the corresponding isolated (0,8)- and (0,16)-SWBNNTs is 143 cm^{-1}. A tentative fitting equation may be obtained as given in Equation 4a-b:

$$\omega_{\text{inner}}(\text{RBM, in cm}^{-1}) = \frac{181.27}{d_t\,(nm)} + \frac{37.00}{[\text{d}_\text{t}\,(\text{nm})]^2} - \frac{4.82}{[\text{d}_\text{t}\,(\text{nm})]^3} \qquad a$$

$$\omega_{\text{outer}}\left(\text{RBM, in cm}^{-1}\right) = \frac{237.34}{d_t\,(nm)} + \frac{65.65}{[\text{d}_\text{t}\,(\text{nm})]^2} - \frac{51.85}{[\text{d}_\text{t}\,(\text{nm})]^3} \qquad b \tag{4}$$

where d_t stand for the shell diameter. The tentative fitting equations reproduced calculated RBMs within 0.5 cm^{-1} error range for both inner- and outer-tubes. Another Raman bands below RBM modes in the spectra of the SWBNNTs are blue-shifted relative to the corresponding peaks in the spectra of their corresponding DWBNNTs. For instance, these Raman

features at 147 cm^{-1} in the spectra of (0,8)-SWBNNT and at 130 cm^{-1} in the spectrum of the (0,16)-SWBNNT are respectively blue-shifted to 170 and 139 cm^{-1} in the spectrum of the (0,8)&(0,16)-DWBNNT. Furthermore, in the mid-frequency region, the relatively weak intense peaks are centered 1036 (A_{1g}), 1030 (E_{2g}) and 823 (A_{1g}) cm^{-1} are predicted almost at the same positions in the spectra of both (0,8)- and (0,16)-SWBNNTs.

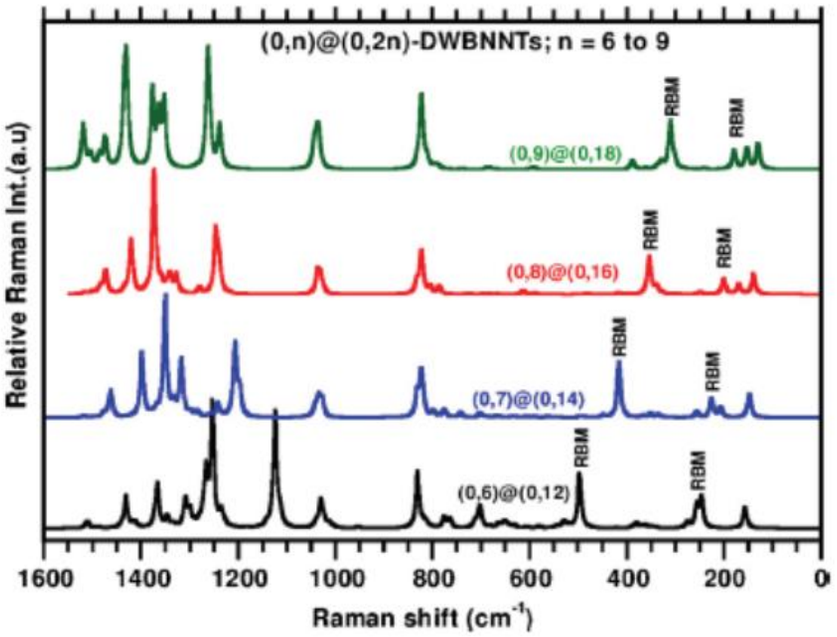

Figure 6. Calculated Raman spectra of the (0,n)&(0,2n)-DWBNNT, n = 0–9.

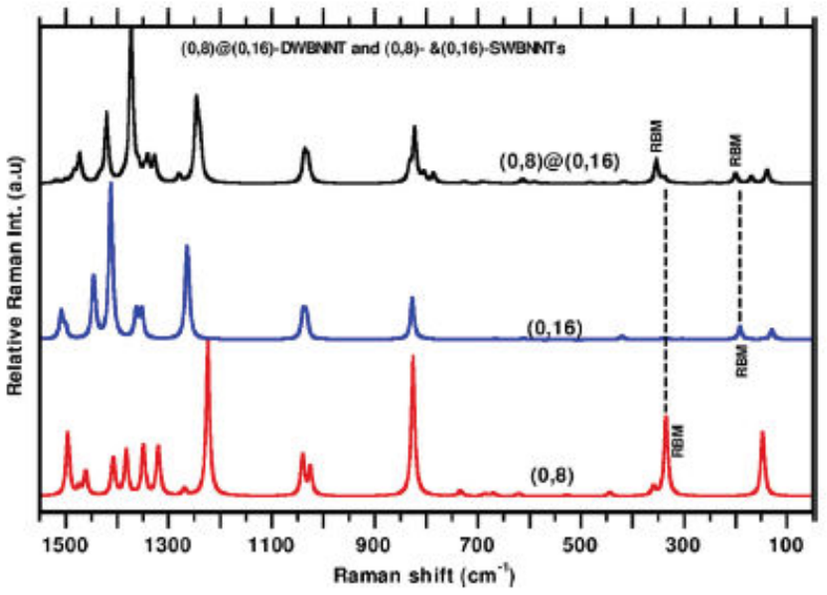

Figure 7. Calculated Raman spectra of the (0,8)&(0,16)-DWBNNT and (0,8)- and (0,16)-SWBNNTs.

http://dx.doi.org/10.5772/51486

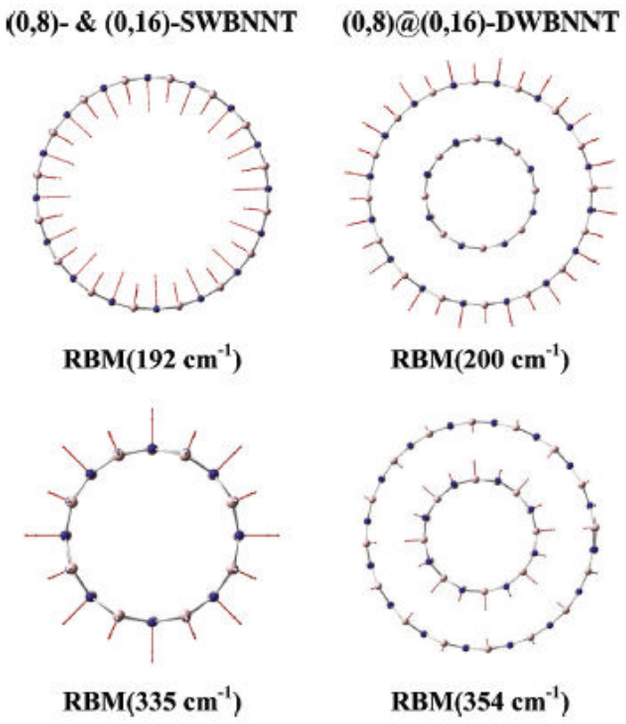

Figure 8. Calculated molecular motions for some vibrational bands of the (0,8)&(0,16)-DWBNNTs and (0,8)- and (0,16)-SWBNNTs.

In the high frequency region, comparing the Raman features in the spectra of the (0,8)&(0,16)-DWBNNTs with their band position in the corresponding (0,n)-SWBNNTs spectra, it can be seen that they are slightly shifted relative to SWBNNTs, as seen in Figure 7 for the (0,8)&(0,16)-DWBNNT. For instance, the Raman bands at 1434 (A_{1g}, relatively weak), 1420 (E_{1g}, medium intense), 1373 (E_{1g}, the most stronger one), 1358 (A_{1g}, relatively weak), and 1246 (E_{1g}, relatively strong) cm^{-1} in the spectrum of the (0,8)&(0,16)-DWBNNT correspond to the Raman features at 1461 (medium), 1407 (medium), 1382 (medium), 1349 (medium), and 1223 (the most stronger) cm^{-1} in the spectrum of the (0,8)-SWBNNT, and these are predicted at 1501 (relatively weak), 1443 (medium), 1412 (the most stronger), 1363 (relatively weak), and 1265 (relatively strong) cm^{-1} in the spectrum of the (0,16)-SWBNNT (see Figure 6), respectively.

Moreover, Y. Bando et. al. [62] have studied Raman spectra of the multi-walled boron (natural ^{11}B and isotope ^{10}B) nitride nanotubes (MWBNNT and MW^{10}BNNT). Their Raman spectra of the MWBNNT and MW^{10}BNNT showed only one strong Raman peak at 1366 and 1390 cm^{-1}, respectively, in the range of 1200 to 1500 cm^{-1}, which is assigned to a BN stretching deformation vibration mode. This measured Raman peak is in good agreement with our calculated Raman peak (E_{1g}) at 1373 cm^{-1} in the calculated nonresonance Raman spectrum of the (0,8)&(0,16)-DWBNNT, which is resulting from the BN stretching along tube axis, including bending deformation of the NBN/BNB bonds along tube axis. Additionally, Obraztsova and coworkers [63] have studied comparative Raman spectra of the multi-walled boron nitride

nanotubes (MWBNNTs) samples before and after Al ion modifications have been investigated. Two features in the Raman spectra were observed: one at 1366 cm^{-1} that corresponds to in-plane vibrations between B and N atoms and broad feature around 1293 cm^{-1} in the spectrum of the Al-modified MWBNNTs. The broad peak around 1293 cm^{-1} is consistent with the calculated Raman feature around 1250 cm^{-1} in the spectra of the DW- and SW-BNNTs.

3.3. IR Spectra of Single-Walled and Double-Walled Boron Nitride Nanotube

Zigzag-SWBNNTs: Figure 9A provides calculated IR spectra for the (n,0)-SWNTs, where n ranges from 6 to 19. As evidenced in Figure 9, the calculated IR spectra exhibited seven peaks of symmetries E_1u and A_{1u} are slightly depend on the SWBNNTs diameter. In the range of 1000 to 1550 cm^{-1}, relatively very weak six IR features of symmetries E_{1u} are centered: ~ 1475 ± 25, ~1330 ± 30, ~1230 ± 30, ~1030 ± 5 cm^{-1}, and other two weak peaks with symmetry A_{1u} are centered ~1495 ± 15 and ~1350 ± 15 cm^{-1}. The strongest one with symmetry E_{1u} is centered 1395 ± 30 cm^{-1}. In the range of mid frequency, the calculated IR spectra of the (0,n)-SWBNNTs (n= 6 to 19) exhibited only one weak peak centered 805 ± 15 cm^{-1}. The analytical expressions for this calculated high frequency band as functions of third order in inverse of the (0,n)-SWBNNTs diameter are given by the equations: $\omega(cm^{-1}) = A + \frac{B}{d_t(nm)} + \frac{C}{\left[d_t(nm)\right]^2} + \frac{D}{\left[d_t(nm)\right]^3}$, where the parameters A(in cm^{-1}), B(in cm^{-1}.nm), C(in cm^{-1}.nm^2) and D(in cm^{-1}.nm^3) are respectively obtained such as: 1508.9, 10.3, -15.6, and 2.4 for the peak (A_{1u}) centered 1495 ± 15 cm^{-1}; 1515.7, -14.9, -2.4, and -3.6 for the peak (E_{1u}) centered 1475 ± 25 cm^{-1}; 1344.7, 130.0, -54.1, and -2.4 for the peak (E_{1u}) centered 1395 ± 30 cm^{-1}; 1357.2, 33.7, -41.0, and 10.2 for the peak (A_{1u}) centered 1350 ± 15 cm^{-1}; 1367.0, -4.9, -17.4, and 0.8 for the peak (E_{1u}) centered 1330 ± 30 cm^{-1}; 1264, 23.2, -37.3, and 3.8 for the peak (E_{1u}) centered 1230 ± 30 cm^{-1}; 1030.5, 28.6, -31.4, and 9.1 for the peak (E_{1u}) centered 1030 ± 5 cm^{-1}; and 824.8, 7.5, -22.3, and 4.1 for the peak (E_{1u}) centered 805 ± 15 cm^{-1}. The plots of the calculated IR features vs. inverse of the tube diameter are given in Figure 9B. In the low frequency region, the IR spectra exhibited many IR features; however, their intensities are extremely weak or vanish as seen in Figure 9A. Furthermore, we provided the vibrational mode assignments and frequencies for the IR spectra of the isolated zigzag-SWBNNTs in Tables 2.

DWBNNTs: While Figure 10 provides the calculated IR spectra for the (0,n)&(0,2n)-DWBNNTs, with n ranging from 6 to 9; Figure 11 provides calculated IR spectra of the (0,8)&(0,16)-DWBNNTs and isolated (0,8)- and (0,16)-SWBNNTs for comparison. The calculated spectra of the DWBNNTs 1517 (A_{1u}), 1474 (E_{1u}), 1434 (E_{1u}), 1373 (E_{1u}), 1347 (A_{1u}), 1238 (E_{1u}), 823 (E_{1u}) and 786 (E_{1u}) cm^{-1}, which are correspond the IR features at 1496, 1473, 1407, 1320, 1349, 1224, and 798 cm^{-1} in the spectrum of the (0,8)-SWBNNT; these are calculated at 1509, 1501, 1412, 1353, 1363, 1261, and 819 cm^{-1} in the spectrum of the (0,16)-SWBNNT, as seen in Table 2. Moreover, Y. Bando [62] have studied FTIR spectra of the multi-walled boron (natural ^{11}B and isotope ^{10}B) nitride nanotubes (MWBNNT and $MW^{10}BNNT$). Their FTIR spectra of the MWBNNT and $MW^{10}BNNT$ revealed blue degraded strong IR peak at 1376 and 1392 cm^{-1}, respectively, which is assigned to a B-N stretching deformation vibration mode. This measured IR peak is in good agreement with our calculated IR peaks at 1367

http://dx.doi.org/10.5772/51486

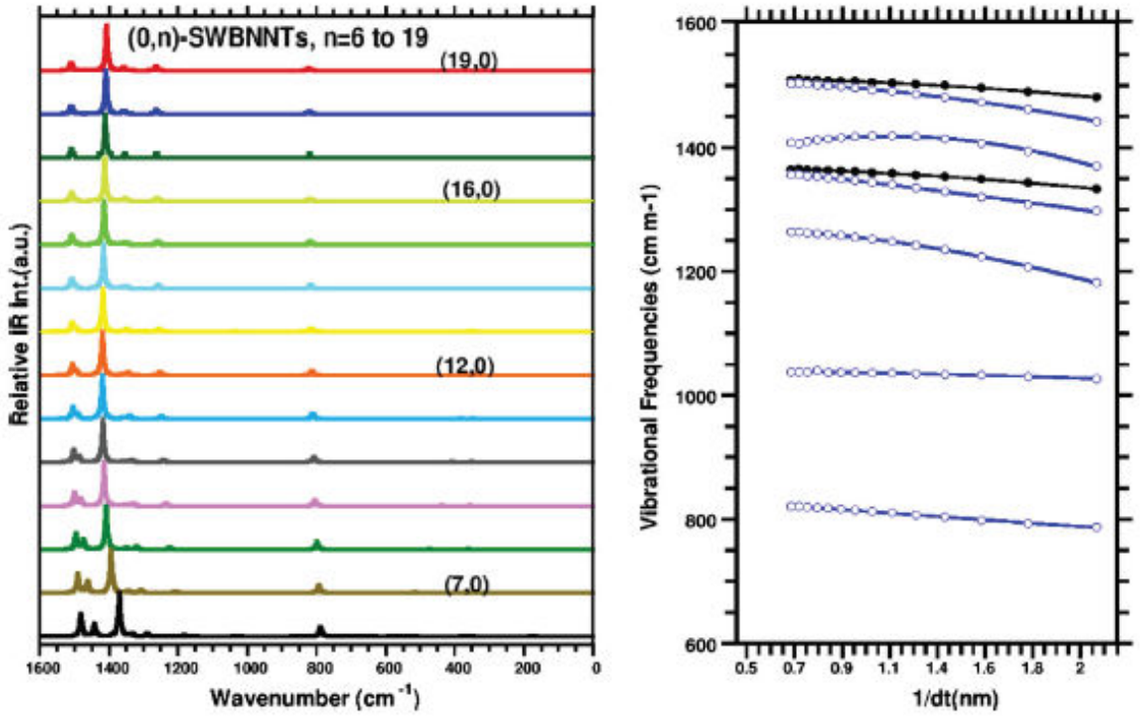

Figure 9. (A) calculated IR spectra of the (0,n)-SWBNNTs, n = 6–19 and (B) the plots of the frequencies of vibrational modes versus $1/d_t$.

cm^{-1} (E_{1u}, resulting from the bending deformation of the NBN/BNB bonds along tube axis) and 1424 cm^{-1} (E_{1u}, due to the BN stretching along tube axis, including bending deformations of NBN/BNB bonds). Author also observed a relatively weak and broad IR features at ~800 cm^{-1} and suggested that this IR peak is due to the existence of some B-O bonds in their BN nanotubes, see Figure 4 in Ref. [62]. However, our calculated IR spectra of the SWBNNTs and DWBNNTs exhibited IR feature with relatively weak around 800 cm^{-1} is as a result of the out-of surface bending deformation of NBN/BNB bonds on the boron nitride nanotube. Therefore, we suggest that this IR peak (~800 cm^{-1}) may originate from the boron nitride nanotube.

3.4. Electronic transition energies of DWBNNT and SWBNNTs

As mentioned in the introduction to this section, boron nitride nanotubes (BNNTs) can be viewed as modified CNT, but their electronic properties differ from carbon nanotubes. For instance, depending on their chirality and the radius, although carbon nanotubes can be either metallic or semiconducting, all boron nitride nanotubes (BNNTs) are semiconducting materials with a large band. And since the band gap is large, the gap energy is only weakly dependent on the diameter, chirality, and the number of the walls of the tube. Furthermore, owing to their semiconducting character, BNNTs, like CNTs, themselves are also very interesting materials for application in nanoscale devices, and have been considered alternatives to CNTs. The DWBNNTs as well as the doped BNNTs nanotubes may show a dramatic change relative to the isolated nanotube. On account of the strong interactions between elec-

	(0,6)	(0,7)	(0,8)	(0,9)	(0,10)	(0,11)	(0,12)	(0,13)	(0,14)	(0,15)	(0,16)	(0,17)	(0,18)	(0,19)	(0,6)& (0,12)	(0,7)& (0,14)	(0,8)& (0,16)	(0,9)& (0,18)
E_{1u}	788	793	798	804	807	811	813	815	817	818	819	820	821	821	764 813	775 820	786 823	795 824
	Out-of-surface bending deformation of the NBN/BNB bonds on the tube																	
E_{1u}	1182	1207	1224	1235	1242	1248	1252	1255	1258	1260	1261	1262	1264	1264	1253	1197	1238	1257
	Asymmetric stretching vibrations of the NBN/BNB bonds due to the motions of the N and B atoms along circumference direction.																	
E_{1u}	1298	1308	1320	1329	1335	1340	1344	1347	1349	1351	1353	1354	1356	1356	1366	1351	1373	1376
	Bending deformation of the NBN/BNB bonds, including relatively weak BN bond stretching																	
A_{1u}	1333	1343	1349	1353	1355	1358	1359	1361	1362	1363	1363	1364	1364	1365	1332	1332	1347	1363
	BN stretching and bending deformation of the NBN/BNB bonds along tube axis																	
E_{1u}	1370	1394	1407	1414	1418	1419	1419	1418	1416	1414	1412	1410	1408	1406	1439	1433	1434	1429
	Asymmetric stretching vibrations and bending deformations of the BNB/NBN bonds.																	
E_{1u}	1442	1462	1473	1481	1486	1491	1493	1496	1498	1499	1501	1502	1503	1504	1488	1466	1474	1476
	BN stretching, including bending deformations of NBN/BNB bonds																	
$A1_u$	1481	1490	1496	1500	1502	1504	1505	1507	1507	1508	1509	1509	1509	1510	1511	1517	1517	1519
	BN stretching along tube axis, including bending deformations of NBN/BNB bonds																	

Table 2. DFT-calculated IR vibrational frequencies (in cm^{-1}) and assignments for (0,n)-SWBNNT and (0,n)&(0,2n)-DWBNNTs at the B3LYP/6-31G level.

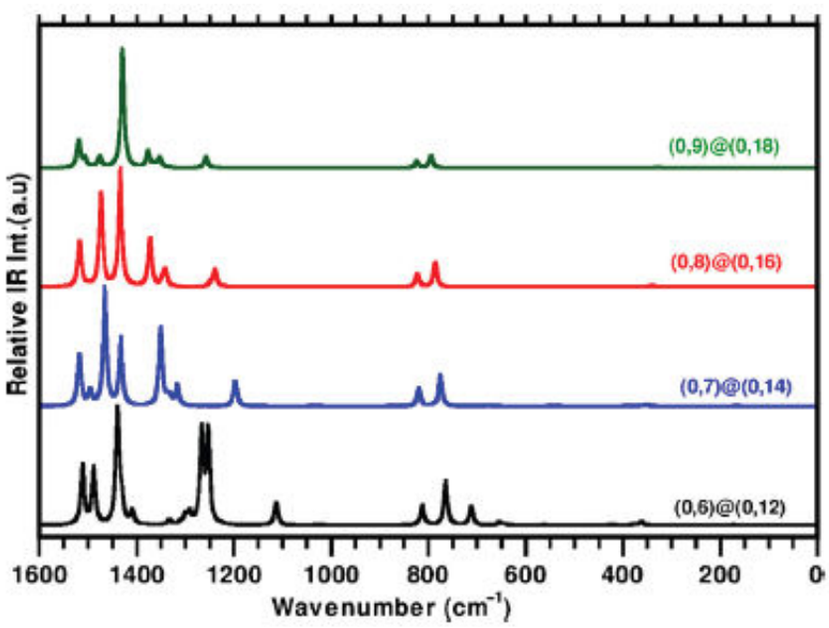

Figure 10. Calculated IR spectra of the (0,n)&(0,2n)-DWBNNT, n = 6–9.

http://dx.doi.org/10.5772/51486

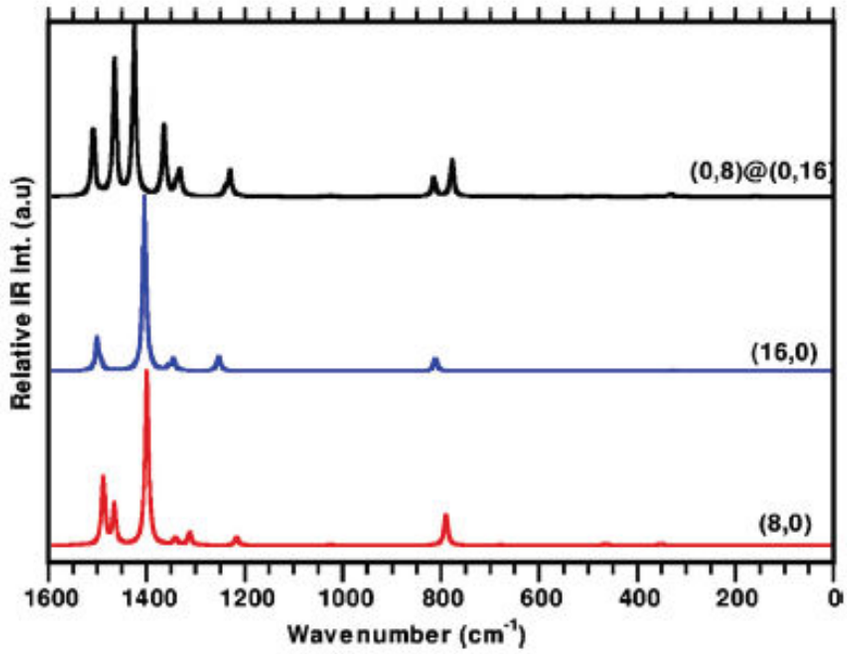

Figure 11. Calculated IR spectra of the (0,8)&(0,16)-DWBNNT and (0,8)- and (0,16)-SWBNNTs for comparison.

trons and holes in DWBNNTs, the excitonic effects in BNNTs is expected to be more important than in CNTs, since bright (dipole allowed) and dark (dipole forbidden) excitons in DWBNNTs can exhibit qualitatively different optical response. Therefore, the time-dependent DFT (i.e., TD-DFT) method has been applied to investigate the dark transient structures involved in radiationless processes for the DWBNNTs. In this section, we provide the calculated vertical electronic transitions of (0,6)&(0,12)-DWBNNT and (0,6)- and (0,12)-SWBNNTs using DFT and discuss these results in terms of IC and ISC processes.

The calculated vertical electronic transitions of (0,6)&(0,12)-DWBNNT and (0,6)- and (0,12)-SWBNNTs, as seen in Figure 12 and Table 3, indicated that the lowest electronic energy level (dipole forbidden) of the DWBNNTs are lower as much as about 0.4 eV relative to the (0,6)-SWBNNT and 1.5 eV relative to the (0,12)-SWBNNT. However, when we compare the lowest dipole allowed electronic transitions, the lowest dipole allowed electronic transitions of the DWBNNT are about 1.07 eV and 0.99 eV lower than that for (0,6)- and (0,12)-SWBNNTs, respectively.

The predicted dipole allowed electronc transitions, $S_0(A') \rightarrow S_7(A'')$ (4.90 eV) and $S_0(A') \rightarrow S_8(A')$ (4.91 eV), respectively,are due to the HOMO-4(A″)→LUMO(A′) and HOMO-5(A′) →LUMO(A′) transitions; $S_0(A') \rightarrow S_{10}(A'')$ (4.94 eV) is as a result of HOMO-6(A″)→LUMO(A′) transition; $S_0(A') \rightarrow S_{11}(A'')$ (5.12 eV) is mainly due to HOMO(A″)→LUMO+4(A″) and HOMO-3(A′)→LUMO+2(A′)transitions and $S_0(A') \rightarrow S_{12}(A'')$ (5.12 eV) is mainly because of HOMO-3(A′)→LUMO+1(A″) and HOMO(A″)→LUMO+5(A′) transitions. These calculated transitions, together with the plotted electron densities in the HOMOs and LUMOs, as seen in Figure 4B, indicated that first three of five dipole allowed electronic transitions of the

(0,6)&(0,12)-DWBNNT							(0,12)-SWBNNT			(0,6)-SWBNNT		
$S_0 \rightarrow S_n$				T1→Tn (SCF Corrected)			$S_0 \rightarrow S_n$			$S_0 \rightarrow S_n$		
Exc. St.#	Sym.	eV	f	SYM.	eV	f	Sym.	eV	f	Sym.	eV	f
1:	A"	4.35		A"	4.24		E_1	5.83		A"	4.72	
2:	A'	4.47		A'	4.59	0.0071	E_1	5.95		A'	4.86	
3:	A"	4.67		A"	4.59	0.0072	E_1	5.95		A"	4.86	
4:	A'	4.67		A"	4.93	0.0006	E_1	5.97	0.0871	A'	4.86	
5:	A'	4.89		A'	4.93	0.0007	E_1	5.97	0.0871	A"	5.71	
6:	A"	4.89		A'	4.96		E_1	6.01	0.0239	A'	5.71	
7:	A"	4.90	0.0334	A"	4.96		E_2	6.19		A'	5.83	
8:	A'	4.91	0.0331	A"	4.98		E_2	6.19		A'	5.89	0.0001
9:	A'	4.93		A'	5.01		E_1	6.30	0.8777	A"	5.89	0.0129
10:	A"	4.94	0.0003	A"	5.24		E_1	6.30	0.8777	A"	5.90	0.0316
11:	A'	5.12	0.0055	A'	5.24		A_1	6.36	0.0256	A'	5.90	0.0443
12:	A"	5.12	0.0058	A'	5.27	0.0088	E_1	6.39	0.0168	A"	5.94	0.0002
13:	A"	5.21		A"	5.27	0.0091	E_1	6.39	0.0168	A"	6.05	
14:	A'	5.21		A'	5.44	0.0251	A_2	6.43		A'	6.11	0.0062
15:	A"	5.25		A"	5.44	0.0234	E_2	6.51	0.5031	A"	6.11	0.0063
16:	A'	5.25		A'	5.52	0.0022	E_2	6.51	0.5031	A'	6.20	0.0001
17:	A"	5.26		A'	5.56		E_2	6.52		A"	6.20	0.0001
18:	A"	5.30		A"	5.65		E_2	6.52		A'	6.26	0.0092
19:	A'	5.37		A"	5.67		E_1	6.60	0.0012	A'	6.38	
20:	A"	5.37		A'	5.68		E_1	6.60	0.0012	A"	6.38	

Table 3. The calculated vertical electronic transitions, singlet-singlet ($S_0 \rightarrow S_n$ and triplet-triplet ($T_1 \rightarrow T_n$), of the (12,0)&(6,0)-DWBNNT and (12,0)- and (6,0)-SWBNNTs for comparison at the B3LYP/6-31G level of using DFT. Note that the SCF corrected triplet-triplet electronic transitions were calculated as the deference between the calculated global energies of the singlet and triplet sates added to triplet-triplet electronic transitions in order to comparing with the singlet-singlet transitions and where the letters S_0, T_1 and f are respectively the lowest energy level of the singlet, triplet states and oscillator strength.

http://dx.doi.org/10.5772/51486

(0,6)&(0,12)-DWBNNT, $S_0(A') \rightarrow S_7(A'')$/ $S_8(A')$/ $S_{10}(A')$, originating from the electron transfer from the outer-shell to the inner-shell. These results are clear evidence of the charge transfer from the other shell to the inner shell. The dipole allowed electronic transitions $S_0(A') \rightarrow S_{11}(A')$ shows the electron excited from both inner- and other-shells to mostly inner shells, also there is a significant sigma-bonding interactions between inner- and outher-shells. Finally, the $S_0(A') \rightarrow S_{11}(A')$ transition indicate that the transitions from both shells to the excited state mainly are due to sigma-bonding interactions. We also calculated the triplet-triplet transitions, which produce many dipole allowed transitions. The SCF corrected electronic transitions of the singlet-singlet and triplet-trpilet of the (0,6)&(0,12)-DWBNNT, together with the singlet-singlet transitions, are given in Figure 12. As seen in Figure 12 and Table 3, upon irradiation, there is the possibility of a system that can undergo internal conversion (IC) and intersystem crossing (ISC) processes via vibroelectronic coupling, besides the photochemical and other photophysical processes. The IC and ISC processes would able to be expected when taking account of the small distance between the electronic energy levels and range of the vibrational spectra of the DWBNNTs.

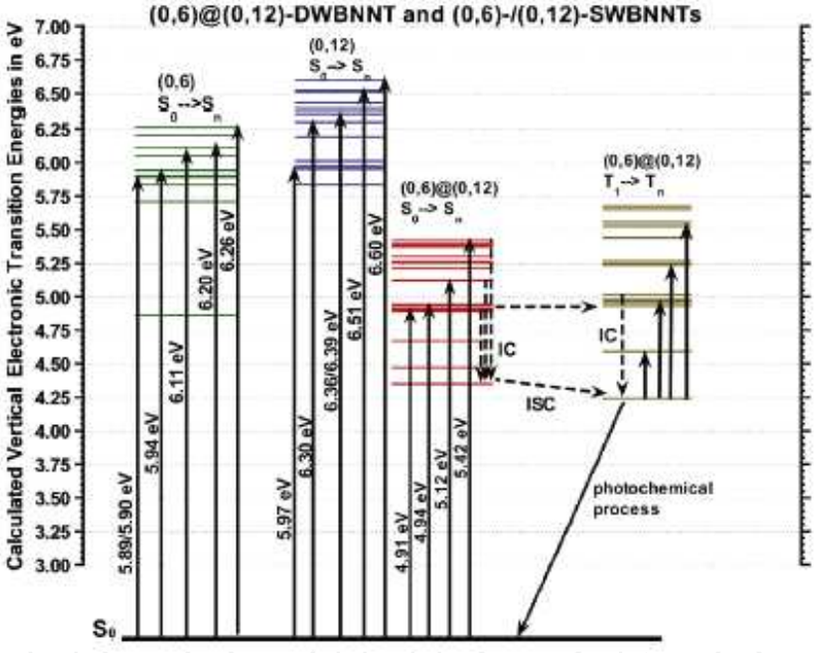

Figure 12. Calculated vertical electronic transitions, singlet–singlet (S0→Sn and triplet–triplet (T1→Tn) for (0,6)&(0,12)-DWBNNT and (0,6)- and (0,12)-SWBNNTs. The vertically solid arrow indicated dipole allowed transitions. The broken-arrows display possible internal conversion (IC) and intersystem crossing (ISC) processes.

C. H. Lee and coworkers [64] have measured absorption spectrum of the suspension of BNNTs in ethanol by using UV–visible absorption spectroscopy (HP 8453 Spectrophotometer). The authors observed three absorption bands at ~5.9 eV (very strong) and ~4.78 eV (weak), and ~3.7 eV (very weak) in the UV-visible spectrum and suggested that the band at about 4.75 eV originates from the intrinsic dark exciton absorption band; the relatively small band at ~ 3.7 eV was due to the defects of the boron nitride nanotubes (BNNTs), and the

stronger band at 5.9 eV was as results of the optical band gap of BNNTs. For the (0,6)&(0,12)-DWBNNT, as seen in Table 3, our calculated electronic transitions produced a few dipole allowed electronic transitions below 5.37 eV such as: $S_0 \rightarrow S_7/S_8$ at 4.90 eV (with the f = 0.0334), $S_0 \rightarrow S_{10}$ at 4.94 eV (f = 0.0003), $S_0 \rightarrow S_{11}/S_{12}$ at 5.25 eV (f = 0.0055), which are in good agreement with this measured band at about 4.78 eV. Furthermore, for the (0,6)- and (0,12)-SWBNNTs, the calculations exhibited the lowest dipole allowed electronic transition around 5.9 eV, which is in accordance with the measured strong optical band at 5.9 eV. The lowest dipole forbidden transitions are predicted at 4.35, 4.72, and 5.83 eV for the (0,6)&(0,12)-DWBNNT, (0,6)- and (0,12)-SWBNNTs, respectively. Consequently, this experimentally measured UV-visible spectrum might be an evidence for the formation of the (0,6)&(0,12)-DWBNNT, the observed absorption band (at ~4.78 eV) may due to the $S_0 \rightarrow S_7/S_8$ (4.90 eV), not due to the intrinsic dark exciton as suggested by authors.

Furthermore, Figure 4A provides the calculated electron density of (0,6)&(0,12)-DWCNT (double-walled carbon nanotube), showing that the first four highest occupied molecular orbitals (from HOMO to HOMO-3 with the A_{1u}, A_{2g} and $2E_{1g}$ symmetries, respectively) belong to the outer-shell, and the next highest occupied molecular orbitals from HOMO-4 to HOMO-24 include both inner- and outer-shells of (0,6)&(0,12)-DWCNT. The lowest unoccupied molecular orbital LUMO (E_{1u}), lying about 0.780 eV above the HOMO (A_{1u}), belongs to the outer-shell, while the next one (B_{2u}) belongs to the inner-shell and lies 0.849 eV above the HOMO (A_{1u}). The calculated electron density also indicates that an intratube (inner and outer tube) interaction may possibly take place in the excited state: the LUMO+7 with A_{2u} symmetry and 2.494 eV above the HOMO (A_{1u}), LUMO+8 (E_{1u}; 2.557 eV), LUMO+10 (E_{1g}; 2.563 eV) and LUMO+15 (E_{1g}; 3.637 eV). The intratube CC σ-bonding interaction in the excited state may lead to an intertube charge transfer, which can be observed by a significant change in the tangential modes (TMs) of Raman spectra when the tube is excited to its intratube charge transfer state. The TM may provide information not only about the metallic or semiconducting character of nanotubes, but also on the inner-outer tube (intratube) charge transfer.

Similarly, the calculated vertical electronic transitions for the (0,n)&(0,2n)-DWBNNT and (0,n)- and (0,2n)-SWBNNTs, n= 8 and 9, at the same level of the theory. The calculated singlet-singlet ($S_0 \rightarrow S_n$ and triplet-triplet ($T_1 \rightarrow T_n$) electronic transitions are given in Table 4.

For the (0,8)&(0,16)-DWBNNT, the predicted dipole allowed electronc transitions, $S_0 \rightarrow S_2/ S_3$ (5.39 eV, mainly due to the H-1 →L and H→L) and $S_0 \rightarrow S_6$ (5. 47 eV, mainly due to the H-3 →L). These calculated transitions, in conjunction with the plotted electron densities in the HOMOs and LUMOs, as seen in Figure 4C, indicated that first three dipole allowed electronic transitions of the (0,8)&(0,16)-DWBNNT, $S_0 \rightarrow S_{2/3}/ S_6$ originating from the electron transfer from the outer-shell to the inner-shell. These results of the calculations provide not only clear evidence for the charge transfer from the other shell to the inner shell, but also there is a significant BB σ-bonding interaction between the inner- and outer-shells. As seen in Table 4, the lowest dipole allowed vertical electronic transition of the (0,8)&(0,16)-DWBNNT ($S_0 \rightarrow S_2$; 5.39 eV) lies 0.61 and 0.52 eV below the lowest allowed transitions of the $S_0 \rightarrow S_6$ and $S_0 \rightarrow S_4$ for the (0,8)- and (0,16)-SWBNNTs, respectively.

http://dx.doi.org/10.5772/51486

Furthermore, upon irradiation, a system can undergo internal conversion (IC) and intersystem crossing (ISC) processes, besides the photochemical and other photophysical processes. Transient intermediates are likely to form in the IC and ISC radiationless processes, which is also known as "dark processes". Our calculations also indicated that possibilities of the IC and ISC processes via vibroelectronic coupling, besides the photochemical and other photophysical processes. For instance, based on the calculated electronic transitions as seen in the Table 4, when the (0,8)&(0,16)-DWBNNTs are excited, all of the excited nanotubes may not directly return back to their ground state by emission of a photon, $S_{k>0} \rightarrow S_0$ transition, but some of them may return back to their ground states (S_0) by the IC (internal conversion), for instance, when the system is excited into a higher vibroelectronic state (S_6, 5.47 eV), it may undergo into the S_1 state (5.39 eV) via vibrational coupling between these two states before undergoing additional vibrational relaxation back to the lowest singlet electronic energy level (S_1), which is called internal conversion (IC), then, followed by transition from the second lowest singlet electronic energy level S_1(5.39 eV) to S_0 by emission of a photon is so-called fluorescence. An alternate pathway for a molecule in the S_1 state involves an intersystem crossing (ISC) by the nanotube into the lowest triplet electronic state T_1 (5.28 eV). From T_1, the nanotube can undergo radiative de-excitation via a much slower process, which is known as phosphorescence ($T_1 \rightarrow S_0$ transition) such as illustrated in Figure 12.

Likewise, for the (0,9)&(0,18)-DWBNNT, the calculations indicated that the lowest dipole allowed transition ($S_0 \rightarrow S_3$, 5.69 eV) lies 0. 18 and 0.21 eV below the lowest allowed transitions of the (0,9)- and (0,18)-SWBNNT. Additionally, as seen in Table 4, the calculations also indicated that the possibilities of the IC from the S_k (k=3,4,7-9, and 14) to S_1 as well as ISC proces from the singlet electronic state S_1(5.67 eV) to T_1 (5.71 eV) for the (0,9)&(0,18)-DWBNNT. The calculated dipole allowed vertical electronic transitions may be summarized as following: the transition $S_0 \rightarrow S_{3/4}$ (5.69 eV and f=0.1656) is predominantly as result of the electron excitation mostly from the outer shell to the inner shell (H→L+1, H-1→L, H-6→L+1/2), including excitations from inner shell to the outer (H-2→L+1/2 and H-3→L+1/2); $S_0 \rightarrow S_7$ (5.73 eV and f=0.0060 is mainly as result of the electronic excitation from the outer shell to the inner shell (H→L+1, H-1→L+2, H-6→L), including relatively weak contribution from inner shell to the outer (H-3→L+5 and H-2→L+6); and the transitions $S_0 \rightarrow S_{8/9}$ (5.74 eV and f=0.0007) and $S_0 \rightarrow S_{14}$ (5.78 eV and f=0.0077) are as result of the electronic excitation from the outer shell to the outer shell (H-5→L+3/4 and H-4→L+3/4), as shown in Figure 4 D.

The key conclusions on the calculated electronic spectra indicates that the first dipole allowed electronic transitions of the (0,n)&(0,2n)-DWBNNTs (n = 6,8, 9) lead to a charge transfer process from outer shell to the inner shell. Moreover, there is a significant intertube σ-bonding interactions between the inner- and outer-shells occurs with decreasing distance between the interwall of the DWBNNTs, in contrast, for the (0,9)&(0,18)-DWBNNT, there is a relatively weak contributions to the charge transfer process from the inner-shell to outer-shell.

	(0,8)&(0,16)-DWBNNT				(0,8)-SWBNNT		(0,16)-SWBNNT		(0,9)&(0,18)-DWBNNT				(0,9)-SWBNNT		(0,18)-SWBNNT	
	$S_0 \rightarrow S_n$		$T_1 \rightarrow T_n$		$S_0 \rightarrow S_n$		$S_0 \rightarrow S_n$		$S_0 \rightarrow S_n$		$T_1 \rightarrow T_n$		$S_0 \rightarrow S_n$		$S_0 \rightarrow S_n$	
n	eV	f	eV	f	eV	f	eV	f	eV	f	eV	f	eV	f	eV	f
1	5.39		5.28		5.61		5.79		5.67		5.71		5.77		5.79	
2	5.39	0.1039	5.32	0.0003	5.61		5.88		5.68		5.74	0.0002	5.86		5.87	
3	5.39	0.1039	5.32	0.0003	5.69		5.88		5.69	0.1656	5.77	0.0004	5.86		5.87	
4	5.46		5.37		5.80		5.91	0.1868	5.69	0.1652	5.78		5.87	0.0215	5.90	0.2880
5	5.46		5.37		5.87		5.91	0.1868	5.70		5.85	0.0021	5.87	0.0215	5.90	0.2880
6	5.47	0.0007	5.49		6.00	0.0255	5.94	0.0268	5.70		5.92	0.0002	5.95	0.0135	5.91	
7	5.47		5.50		6.00	0.0255	5.96		5.73	0.0060	5.94	0.0001	6.06		5.91	
8	5.47		5.50		6.02		5.96		5.74	0.0007	5.95	0.0058	6.06		5.93	0.0287
9	5.52		5.67		6.02		6.16	2.0492	5.74	0.0007	6.00	0.0018	6.06		6.06	
10	5.67		5.82	0.0594	6.04		6.16	2.0492	5.76		6.01	0.0038	6.06		6.06	
11	5.67		5.82	0.0594	6.07	0.0164	6.17		5.76		6.07	0.0021	6.09		6.11	2.5027
12	5.67		5.92	0.0167	6.11		6.17		5.78		6.15	0.0077	6.09		6.11	2.5026
13	5.69		5.92	0.0167	6.11		6.27	0.0432	5.78		6.16	0.0049	6.16		6.24	0.0165
14	5.69		5.94		6.14		6.27	0.0432	5.78	0.0077	6.23	0.0151	6.16		6.24	0.0165
15	5.74		6.00		6.14		6.31		5.83		6.24	0.0103	6.28		6.28	
16	5.74		6.00		6.16		6.31		5.83		6.26	0.0215	6.28		6.28	
17			6.03		6.17		6.34	0.0211			6.28	0.0065	6.30	0.0918	6.34	
18					6.18		6.35	0.0587					6.30	0.0918	6.34	
19					6.33	0.2616	6.35	0.0587							6.35	0.0334

Table 4. The calculated vertical electronic transitions, singlet-singlet ($S_0 \rightarrow S_n$ and triplet-triplet ($T_1 \rightarrow T_n$), of the (0,8)&(0,16)-DWBNNT and (12,0)- and (6,0)-SWBNNTs for comparison at the B3LYP/6-31G level of using DFT. Note that the SCF corrected triplet-triplet electronic transitions were calculated as the deference between the calculated global energies of the singlet and triplet sates added to triplet-triplet electronic transitions in order to comparing with the singlet-singlet transitions and where S_0 and T_1 is respectively the lowest energy level of the singlet and triplet states.

4. Covalently functionalized zigzag-SWCNTs

Carbon nanotubes have broad range of potential applications from medical to industry fields due to their unique structural, mechanical, and electronic properties, as mentioned in the introduction section. Different functionalization methods such as chopping,

http://dx.doi.org/10.5772/51486

oxidation, wrapping and irradiation of the CNTs can lead to active bonding sites on the surface of the nanotubes.

In this section, we calculate, for covalently functionalized carbon nanotubes (f-CNTs), such parameters as the curvature energies referenced, IR and Raman spectra, and vertical electronic transitions. The latter one may be important to understand the optical mechanism for the charge transfer between functional group(s) and CNT as well as internal conversion and intersystem crossing, as well photochemical process that may occur.

The structure of the functionalized-single-walled carbon nanotubes, f-(n,0)-SWCNTs, constructed of functional group(s) covalently bound on the (n,0)-SWCNTs,of two unit cell length, has been investigated. The most stable of the geometry has been obtained by full optimization without any symmetry restriction. The optimized structure indicated that the cylindrical shape of the nanotube is altered to an elliptical form when two molecules attached to the surface of CNT; but the structure remains almost cylindrical with C_4 symmetry, when four functional groups are bound. When we used benzenesulfonic acid (ph-SO_3H; $C_6H_5SO_3H$) as a functional group that covalently bonds on the surface of the (n,0)-SWCNTs, n=6 to 12, the curvature energy per hexagon, ($\Delta E[f\text{-}(n,0)\text{-}SWCNTs]$),of the functionalized-(n,0)-SWCNT calculated relative to that of the corresponding isolated species is given by the following equation:

$$\Delta E[\text{f-(n, 0)-SWCNTs; in eV}] = \frac{E[\text{f-(n, 0)-SWCNT}] - E[\text{f}]}{2n} - \frac{E[\text{(n, 0)-SWCNTs}]}{2n} \quad (9)$$

where E[f-(n,0)-SWCNTs], E[f] and E[(n,0)-SWCNTs] indicates the global energy of functionalized-(n,0)-SWCNT, isolated benzenesulfonic acid ($C_6H_5SO_3H$) and isolated (n,0)-SWCNT, respectively,The f and n stand for the functional group and chiral index of the zigzag-CNTs. The plot of the calculated relative curvature energy is given in Figure 13. As seen in the Figure 11, the relative curvature energy for the metallic and semiconducting CNTs are well separated. Based on the predicted value of the energies, the results suggested that the covalently functionalization of the SWCNT, with small diameters, are energetically more stable than that with large diameters for the metallic nanotubes. However, for semiconducting nanotubes, the functionalization of the tube is favorable, but the functionalization of the (11,0)-SWCNT is more favorable than (10,0)-SWCNTs. In order to make a correct overall assessment, we need to more data, at least for semiconducting zig-zag nanotubes.

4.1. Raman spectra of functionalized zigzag-SWCNTs

The calculated nonresonance Raman spectra for the covalently functionalized-(n,0)-SWCNTs with benzenesulfonic acid (-ph-SO3H) and the isolated (n,0)-SWCNTs (where n = 7 to 10), as well as the spectrum of the functionalized (7,0)-SWCNT with the carboxylic acid (-COOH), for comparison, are shown in Figure 14. Because of the similarity of the Raman spectra of the f-SWCNTs, here we only discuss the Raman spectra for the functionalization of the (7,0)-SWCNT with the benzenesulfonic acid and carboxylic acid, and the spectrum of the isolated (7,0)-SWCNT. The Raman spectra of both functionalized (7,0)-SWCNT exhibited

many new features relating to the spectrum of the isolated (7,0)-SWCNT as well as shift in the peak positions. The predicted results are summarized below.

In the low energy region below 600 cm^{-1}, 1) one of the important Raman peak, which is the radial breathing mode (RBM), was predicted at 410 cm^{-1} in the isolated (7,0)-SWCNT shifted not only to 390 and 385 cm^{-1} in the spectra of the (7,0)-SWCNT functionalizes with benzenesulfonic acid and carboxylic acid, respectively, but also enhanced in both spectra; 2) the relatively peaks at 109 and 111 cm^{-1} result from the elliptical deformation of the carbon nanotube are respectively shifted to 75 and 121 cm^{-1} (in the spectrum of the (7,0)-SWCNT functionalizes with benzenesulfonic acid), and to 95 and 134 cm^{-1} in the Raman spectrum of the functionalization of the (7,0)-SWCNT with carboxylic acid, the intensity enhanced in both spectra of the functionalized tube; 3) a doubly degenerated peak predicted at 284 cm^{-1} (as a result of diagonal expansion of the tube) in the Raman spectrum of the isolated tube is split into well separated two peaks and appeared at about 250 and 306 cm^{-1} in the spectrum of each (7,0)-SWCNT functionalizes with benzenesulfonic acid and carboxylic acid; 4) a relatively very weak peak at 500 cm^{-1} in the spectrum of the isolated tube appeared at same position, but its intensity significantly enhanced, in the calculated both Raman spectra of the (7,0)-SWCNT functionalizes with benzenesulfonic acid and carboxylic acid, which is ; 5) many relatively weak Raman features (result from the out-of-plane structural deformation of the functional groups) appeared below 600 cm^{-1} as seen in the Figure 14 and 15. In the range from 600 to 1250 cm^{-1}, the Raman spectra of the f-(n,0)-SWCNT exhibited many relatively medium, weak and very weak new Raman peaks beside the peaks appeared at 760, 794 and 911 (very weak) cm^{-1} in the Raman spectra of the f-(n,0)-SWCNT. For instance, in the Raman spectrum of the (7,0)-SWCNT functionalizes with benzenesulfonic acid, the peaks with relatively intense at 1120 cm^{-1} (due to the structural deformation of the tube, including wagging of CH bonds of the benzene ring); at 1138 cm^{-1} (as a result of asymmetric CSO bond straching and OH bond wagging, including relatively weak bending deformation of the benzene ring); at 1142 cm^{-1} (structural deformation of the tube due to the CC streching, accompanied by wagging of Hs on the benzene ring), and the peak at 1185 cm^{-1} is owing to asymmetric CSO bond stretching and wagging of OH bond. The Raman spectrum of the (7,0)-SWCNT functionalizes with carboxylic acid exhibited relatively strong Raman features at 1122 cm^{-1} (caused by structural deformation of the nanotube, including OH bond wagging); 1146 cm^{-1} (by reason of asymmetric streching of CCO(H) bond, including tube deformation), and the calculated Raman peak at 1181 cm^{-1} is due to asymmetric streching of CCO bonds, including tube deformation. The Raman peaks at 760 cm^{-1} (due to expansion of the tube along the tube axis) and 795 cm^{-1} (as a result of out-of-surface bending deformation of the tube) in the Raman spectrum of the isolated (7,0)-SWCNT at the same positions of the f-SWCNT). A strong peak at around 1225 cm^{-1} in the spectra of the (7,0)-SWCNT and f-(7,0)-SWCNT is completely originates from the wagging of the CH bond at end of the tube. There are also many very weak Raman features appeared in this range from 600 to 1250 cm^{-1}. In the range from 1300 to 1800 cm^{-1}, two peaks at 1300 cm^{-1} (weak) and 1330 cm^{-1} (strong) in the spectrum of the (7,0)-SWCNT functionalizes with benzenesulfonic acid and with carboxylic

http://dx.doi.org/10.5772/51486

acid, as a result of symmetric stretching of CCC bonds and bending deformations along tube axis, which correspond to a relatively weak and doubly degenerate Raman feature at 1305 cm^{-1}. A doubly degenerated peak (relatively very weak) at 411 cm^{-1} (result from asymmetric stretching of CCC bonds within the tube) in the Raman spectrum of the SWCNT is split into two weak peaks at about 1390 and 1405 cm^{-1} in the Raman spectrum of the functionalized (7,0)-SWCNT. The Raman peak with medium intense at 1486 cm^{-1}, resulting from CC bond stretching within the nanotube, corresponds to the peak at ~1504 cm^{-1} in the Raman spectrum of the functionalized (7,0)-SWCNT. The strongest and doubly degenerate Raman peak at 1574 cm^{-1} in the isolated (7,0)-SWCNT, resulting from asymmetric stretching of the CCC bonds along circumference direction of the tube, is blue shifted to nearly degenerated peak at 1590 and 1595 cm^{-1}, as a result of the CC bond stretching within the tube, in the Raman spectra of the f-(7,0)-SWCNT. In this range from 1300 to 1800 cm^{-1}, the Raman spectra of the (7,0)-SWCNT functionalizes with benzenesulfonic acid and with carboxylic acid showed many new Raman features. For example, the strongest peaks appeared at ~1380 and ~1390 cm^{-1} are as a result of asymmetric tube deformation due to the CC bonds stretching, which is not shown in the isolated (7,0)-SWCNT. The peaks at 1373 and 379 cm^{-1} in the spectrum (7,0)-SWCNT functionalizes with benzenesulfonic are mainly due to the asymmetric stretching of the OSO bond and wagging of the OH bond, including asymmetric stretching of the CCC bonds of the benzene ring. The peaks: at 1471 and 1482 cm^{-1}, which is the result of the CC bond stretching within the tube; at , 1548, and 1557 cm^{-1} is due to asymmetric CCC bond stretching within the tube, however, the peak at 1547 cm^{-1} is entirely due to symmetric stretching of the CC bonds of the benzenesulfonic acid . Furthermore, the predicted Raman peak at 1650 cm^{-1} is due to CC bond stretching of the benzene ring, including CH bond wagging on the benzene ring. A very weak peak at 1806 cm^{-1} is as a result of the CO stretching of the carboxylic acid only. As a result of the (7,0)-SWCNT functionalizes with benzenesulfonic acid and with carboxylic acid (f-(7,0)-SWCNT), the key conclusions on these calculated Raman spectra of the f-(7,0)-SWCNT are summarized below: 1) the RBM is red shifted as much as 25 cm^{-1}; 2) many new peaks appeared in the disorder (D) mode range from 1300 to 1450 cm^{-1}, which is due to the structural deformation of the tube and of the functional groups bound to the tube (7,0)-SWCNT); 3) the tangential (or G) mode is blue shifted as much as 20 cm^{-1}, as a result of the functional groups bound to the tube; 4) above the G-mode, appeared new Raman feature in the spectra of the f-(7,0)-SWCNT belong to the functional groups (benzenesulfonic acid and carboxylic acid); 5) the new Raman features are found to appear along the spectrum, which is owing to the combination of the structural deformation of the tube and the functional groups; 6) for the benzenesulfonic acid, while the CH bond stretching mode occurred range from 3200 to 3240 cm^{-1}, the OH bond stretching appear at 3703 cm^{-1}; for the carboxylic acid, the OH bond stretching is predicted at 3678 cm^{-1}; the CH bond stretching of the tube are predicted in the range from 3172 to 3200 cm^{-1}.; 7) the RBMs of frequency in the calculated Raman spectra of the functionalized (n,0)-SWCNT , (n=6 to 11) are slightly red-shifted relative to that for isolated SWCNTs as seen in Figure 15. The relative shift in frequency of the RBM decreases with increasing tube diameter.

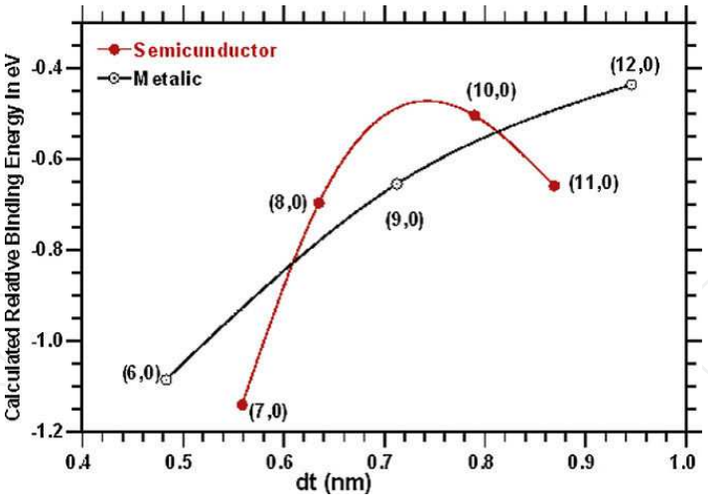

Figure 13. Calculated binding energies of the (n,0)-SWCNTs covalently functionalizes with the benzene sulfonic acid ((n,0)-SWCNTs-ph-SO_3H, n = 6–12). Energetically more stable covalently functionalized (n,0)-SWCNT (f-(n,0)-SWCNTs; n = 6–12) was predicted by using the equation: ΔE[f-(n, 0)-SWCNTs : in eV] = E[f-(n, 0)- SWCNT]/2n – [E(f) + E[(n, 0)-SWCNTs]/2n. Where ΔE[f-(n,0)-SWCNTs] is the energy difference between the total energy of the f-(n,0)-SWCNTs per the number of hexagons in the tube (E[f-(n,0)-SWCNT)/2n]) with reference to the total energy of their corresponding isolated (n,0)-SWCNTs per the number of hexagons in the tube (E[(n,0)-SWCNT)/2n]) and the total energy of the functional groups (E(f)/2n). The letters n and 2n stand for the chiral index of the zigzag-SWCNTs and the number of hexagon in the nanotube, respectively. See Section 3.1 for more detail.

It is worth nothing that the relative intensity of the peaks in the resonance Raman spectra significantly change. Because of the technical difficulty and calculation time, it is very difficult to calculate resonance Raman spectra. Furthermore, in the low frequency region below 600 cm^{-1}, there are many relatively very weak Raman peaks, which result from out-of-plane motion, or twisting of the phenyl group. These types of Raman bands of the functionalizated the CNTs may significantly enhanced in the resonance Raman spectrum (RRS) since there is a significant dipole-dipole interaction between the functional groups. This may play a crucial role and might be used as signature for the alignment of the CNTs in two dimensional networks, but also, the presence of additional bands may lead to the erroneous conclusion that more than one type of SWNT is present in the sample. For instance, the Raman band(s) resulting from out-of-plane motions are dramatically enhanced when dye molecule aggregate, and are referred to as J- or H- type aggregates.[48(a-d)]

New Raman peaks appeared around 1550 cm^{-1} due to the symmetric stretching of the CCC bonds and rocking of CH bonds in phenyl group of the benzenesulfonic acid. Several new Raman peaks result from only benzenesulfonic acid or combination of benzenesulfonic acid and nanotube dispersed throughout the spectrum. The Raman peak resulting from the stretching of CC sigma bonding between benzenesulfonic acid and SWCNTs is very weak and appear at about 1208 cm^{-1}. In the low frequency region, there are many relatively very weak Raman peaks below 600 cm^{-1}, which result from out-of-plane motion, or twisting of the phenyl group. These type of Raman bands of the functionalized-CNTs can play a crucial role and might be used as signature for the alignment of the CNTs in two dimensional networks. For instance, the Raman band(s) resulting from out-off plane motions are dramatically enhanced when dye molecule aggregate, and are refer-

red to as J- or H- type aggregates.[48(a-d)] It is also worth that the calculations produced nonresonance Raman spectra which differ from the resonance Raman spectra in terms of intensity. Furthermore, the CH stretching of the end group of the CNT appear at around 3185 cm^{-1}, the CH stretching of the benzenesulfonic acid and OH stretching of the carboxyl group are, respectively, at about 3590 and 3680 cm^{-1}.

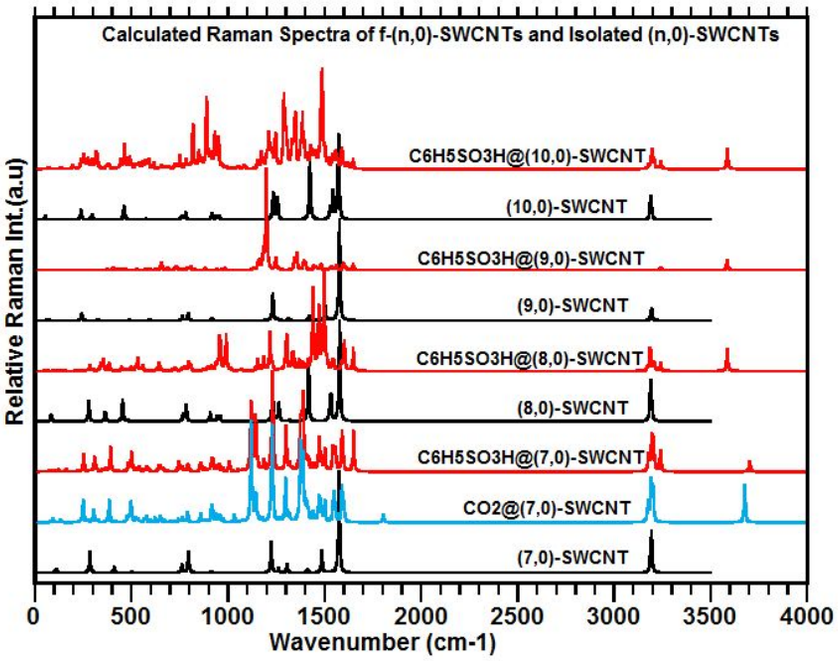

Figure 14. Calculated Raman spectra of the functionalized (n,0)-SWCNTs,benzenesulfonic acid, carboxylic acid, and isolated (n,0)-SWCNTs, n = 7 to 10.

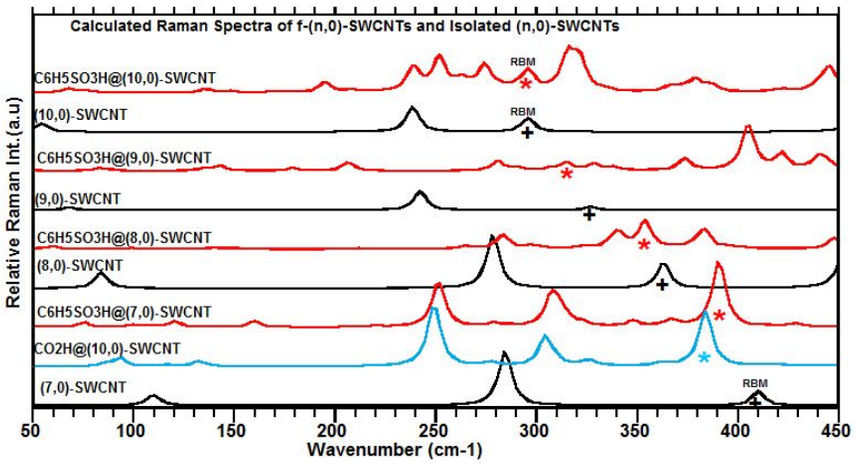

Figure 15. Calculated RBMs of frequencies in Raman spectra of the functionalized (n,0)-SWCNTs with benzenesulfonic acid and carboxylic acid, as well as isolated (n,0)-SWCNTs: n = 7 to 10.

The RBMs of frequency in the calculated Raman spectra of the functionalized SWCNT are slightly red-shifted relative to that for isolated SWCNTs as seen in Figure 15. The relative shift in frequency of the RBM decreases with increasing tube diameter.

4.2. IR spectra of functionalized SWCNTs

As provided in Figure 16, the predicted IR spectra of the (n,0)-SWCNT exhibits strong IR peaks centered at 890 and 845 cm^{-1}; however, the IR spectra of the functionalized (n,0)-SWCNTs display many new strong with relatively weak IR peaks dispersed through spectra, such as at 1650, 1275, 1150, 791, 570, 380, 143 cm^{-1}. Also, in range of 3000-4000 cm^{-1}, the CH and OH stretching modes of the benzenesulfonic acid and carboxylic acid are found to appear at around 1590 and 1670 cm^{-1}, respectively. The C=O bond resulting from C=O stretch of thecarboxyl groups, which is experimentally observed at 1782 cm^{-1} in the FTIR spectra of MWNT, after electron-beam irradiation by Eun-Ju Lee*et al*.[50], is predicted at 1800 cm^{-1} from the calculation.

The peaks found around 1650 cm^{-1} are mainly due to the C-C stretching and CCC bonding deformations; asymmetric and symmetric stretching of the O=S=O group in the benzenesulfonic acid group are found at 1275 and 1150 cm^{-1}, respectively; S-OH stretching appears at 780 cm^{-1}; bending deformation of the SO_3H,mimicking opening and closing of an umbrella,appears at 570 cm^{-1}; out-off plane motion of the phenyl group of the benzenesulfonic acid-appears at 380 cm^{-1}; and twisting of the O=S=O bend appears at about 143 cm^{-1}.

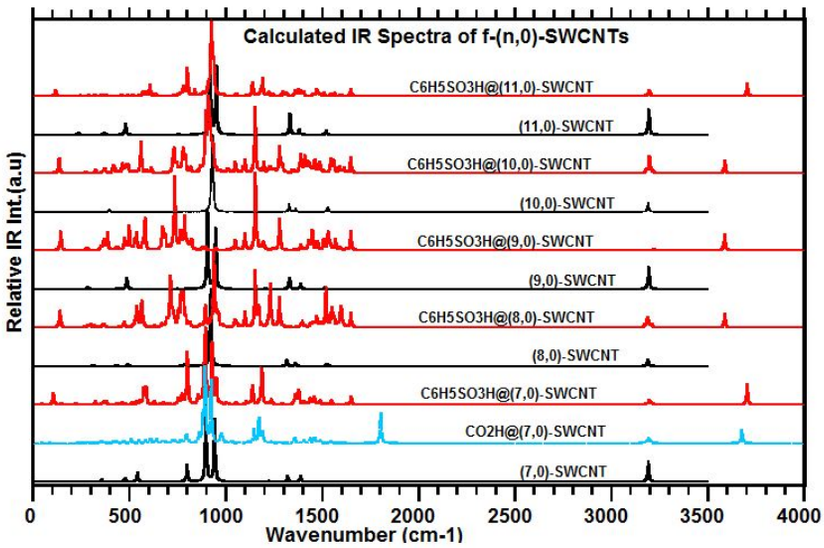

Figure 16. Calculated IR spectra of the (n,0)-SWCNTs functionalized with benzenesulfonic acid, carboxylic acid and isolated (n,0)-SWCNTs: n = 7 to 10.

4.3. Vertical electronic transitions of functionalized SWCNTs

We calculated the vertical electronic transitions for (n,0)-SWCNTs functionalized with benzenesulfonic acid. The functionalized-SWCNTs were constructed as two- and four- func-

tional groups covalently attached to (7,0)/(9,0) and (12,0)/(8,0)-SWCNTs with length equivalent to two unit. Table 5 provides calculated electronic transitions of functionalized and isolated SWCNTs; selected calculated electron density for the HOMOs and LUMOs states involved in the electronic transitions are provided in Figure 17. The results of the calculations clearly indicate that both of the dipole allowed and forbidden electronic transitions are lowered as much as 0.8 eV relative to the transition energies of thecorresponding isolated SWCNT. Furthermore, the calculations also showed that below 2.5 eV there is no electron transfer from the nanotube to the functional group, or vice versa. However, the calculated electronic densities suggest that there would be intrasystem charge transfer between molecule and the nanotube. Because of the distance among the electronic energy levels is very small for some of the dipole allowed and forbidden electronic transitions, radiationless transitions are expected as a result of vibrational coupling or surface touching of the electronic potential energy surfaces. Coupling maybe very large and might lead to internal conversion (IC), again due to vibroelectronic coupling, which might be observable via fluorescence spectroscopic techniques, as discussed and illustrated in Figure 1 in the introduction section. We also would like to point out that while isolated SWCNTs exhibit one or a few dipole allowed electronic transitions below 2.5 eV, the functionalized SWCNTs produced many dipole allowed electronic transitions compared with the corresponding isolated SWCNTs, in addition to lowered electronic transitions.

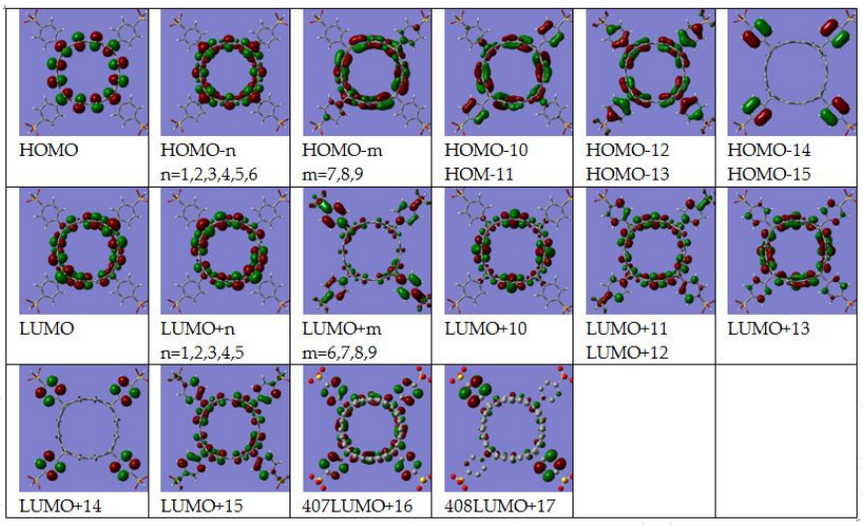

Figure 17. Calculated electron densities in the HOMO and LUMO states for the functionalized (12,0)-SWCNT with benzenesulfonic acid ($C_6H_5SO_3H$).

Calculated vertical electronic transitions, up to 2.53 eV, exhibited many dipole allowed and forbidden electronic transitions. The transitions up to 2.04 eV are due to transitions from the HOMOs of the SWCNT to the LUMO of the SWCNT. Above the 2.04 eV, calculation indicates the existence of charge transfer from the HOMOs of the SWCNT to the LUMOs of the benzenesulfonic acid ($-C_6H_4SO_3H$). For instance, the dipole allowed electronic transitions occur at 2.208, 2.232 and 2.523 eV, as a results of the transitions from the HOMOs of the (12,0)-

SWCNT to the molecule only: H→ L + 8, H→ L + 9 and H-1→ L + 9, respectively. As seen in Table 5, there are many dipole allowed electronic transitions from the HOMO of the SWCNT only to the LUMOs of both SWCNT and the benzenesulfonic acid. The results of the calculated vertical electronic transitions of functionalized nanotube ($C_6H_4SO_3H$@(12,0)-SWCNT) indicate that there is a charge transfer mechanism from the nanotube to the molecule above 2.0 eV. The small distance between the electronic transitions suggest that there would be internal conversion (IC) via vibrational coupling as much as 0.43 eVwhen taking account of the spectral range of the vibrational spectrum of the functionalized nanotube. These spectroscopic properties can be observable by quenching of the fluorescence and by Raman and IR spectroscopy. For the ($C_6H_4SO_3H$@(12,0)-SWCNT, the calculated electronic transitions up to 2.41 eV does not indicate any charge transfer process. However, when one examines the calculated energy levels of the HOMOs and the LUMOs it is possible for charge transfer processes to occur above 2.41 eV.

$S_0 \rightarrow S_k$	(12,0)-SWCNT		4F-(12,0)-SWCNT		(8,0)-SWCNT		4F-(8,0)-SWCNT	
k	T_e(eV)	f	T_e(eV)	f	T_e(eV)	f	T_e(eV)	f
1	0.54	0.0076	0.12	0.0001	0.77	0.0164	0.09	0.0001
2	0.82		0.15	0.0001	1.46	0.0006	0.11	
3	0.82		0.16	0.0001	1.46	0.0006	0.14	
4	1.27		0.42		2.44		0.31	0.0003
5	1.51		0.55	0.0111	2.51	0.3588	0.36	0.0059
6	1.51		0.55	0.0113	2.51	0.3588	0.55	0.0013
7	1.71	0.1082	0.65	0.0355	2.53		0.62	
8	1.87	0.6641	0.65	0.0355	2.77		0.79	
9	1.87	0.6641	0.74	0.0098	2.77		0.93	0.0462
10	2.31		1.10	0.0054	2.78		1.86	0.0049
11	2.31		1.10	0.0053	2.78		1.91	
12	2.56		1.37	0.0072	2.98	0.1295	1.96	0.0022
13	2.76		1.37	0.0071			2.00	
14	2.76		1.49				2.09	0.0002
15	2.81		1.50				2.12	0.0010
16	2.82		1.52	0.0059			2.18	
17	2.82		1.55				2.21	0.0031
18	2.94		1.63	0.0138			2.24	0.0043
19	2.94		1.63	0.0137			2.27	0.0236
20	2.99		1.70	0.0014			2.29	0.0157

21	2.99		1.70	0.0013			2.30	
22	3.03		1.78				2.36	0.0018
23	3.03		1.89				2.38	
24	3.18	0.0301	2.05	0.2005			2.41	0.0015

$S_0 \rightarrow S_k$	(9,0)-SWCNT		2F-(9,0)-SWCNT		(7,0)-SWCNT		2F-(7,0)-SWCNT	
k	T_e(eV)	f	T_e(eV)	f	T_e(eV)	f	T_e(eV)	f
1	0.56		0.27		0.91		0.39	
2	0.80		0.30	0.0144	1.25		0.79	0.0573
3	0.80		0.57		1.25		1.07	0.0067
4	0.93	0.0391	0.83	0.0087	1.45	0.0647	1.11	
5	2.32		1.34		2.52			
6	2.32		1.46	0.0307	2.53			
7	2.50		1.47	0.1432	2.93			
8	2.50		1.57		2.93			
9	2.64		1.64		3.02			
10	2.64		1.84		3.02			
11	2.72		1.88		3.08			
12	2.72		1.88	0.0268	3.08			
13			2.10					
14			2.11	0.0020				
15			2.19					
16			2.24	0.0272				

Table 5. Calculated vertical electronic transition energies (Te; in eV), $S_0 \rightarrow S_k$, of the mF-(n,0)-SWCNTs with that for the isolated (n,0)-SWCNTs for comparison with their oscillator strengths (f). Where m indicated the number of functional groups covalently bound to the (n,0)-SWCNTs and F symbolizes the benzenesulfonic acid used as functional group in this study.

5. Study of polyynes encapsulated into single-walled carbon nanotube

One-dimensional carbon atomic wires displaying sp hybridization have an attractive electronic and vibrational structure which severely affects their optical and transport properties. These kinds of structure have received researchers' interest because of their purely *sp*-hybridized carbon structure that is expected to display a completely different behavior than the more common sp^2 and sp^3 carbon structures. Polyyne molecules are linear carbon chains having alternating single and triple bonds, and ended by end atoms or groups. A. Milani et al. [51] have investigated the charge transfer in carbon atomic wires (polyynes) terminated

by phenyl rings and its effects on the structure of the system using normal Raman and surface-enhanced Raman spectroscopy (SERS) techniques as well density functional theory (DFT) calculations forthe Raman modes. They reported that the occurrence of a charge transfer between polyynes and metal nanoparticles (both in liquids and supported on surfaces) is evidenced by Raman and SERS as a moderating of the vibrational stretching modes. They suggested that carbon wires alter their structure toward a more equalized geometry (i.e., all double bonds) as a consequence of the charge transfer. They also pointed out that these observations open potential perspectives for developing carbon-based atomic devices with tunable electronic properties. Therefore, it is necessary to carry out more experimental and theoretical investigation to get insight of them.

Even though the molecules like polyyne are very unstable at normal temperature and atmosphere conditions.[52, 53], it has beenreported that they are astoundingly stable inside single wall carbon nanotubes (SWCNT) even at high temperature (300 ^{o}C) [54, 55]. The Raman spectrum of the polyyne molecules exhibited two intense Raman shifts appear around 2000 -2200 cm^{-1}, which are labeled as α-bands and β-bands. The band positions of these two bands decrease in frequency with the increase in polyyne size. With the increasing chain lengths, while the frequency of the α-band almost linearly decreases, the position of β-bands is oscillating, and the difference between β-bands and α-bands in frequency shifts are dissimilar in polyyne molecules with different size.

Furthermore, L. M. Malard et al. [56] studied resonance Raman study of two polyyne molecules ($C_{10}H_2$ and $C_{12}H_2$) encapsulated inside the SWCNT using various different laser lines including the whole visible range. They indicated that the main Raman features associated with stretching modes of the linear chains in both samples ($C_{10}H_2$ @SWCNT and $C_{12}H_2$ @SWCNT) are strongly enhanced around 2.1 eV, while the optical absorption observed when these molecules are dispersed in isotropic medium [57] or in the gas phase[58] occurs above 4.5 eV. They concluded that dipole-forbidden (dark) transitions of the polyynes that become active as a result of a symmetry breaking when the molecules are encapsulated inside the SWCNT.

In this section, we will discuss the calculated results for the polyyne ($C_{10}H_2$) molecules encapsulated within (6,0)-SWCNT. Figure 18 and Table 6 provide the calculated electron density and energy levels of the molecular orbitals (MOs), HOMOs and LUMOs, of $C_{10}H_2$@(6,0)-SWCNT, respectively. The geometry optimization with/without symmetry restriction found the point group is respectively D_{6H} and D_{2H} symmetries. The structure with D_{2H} has the lowest energy as much as 0.19 eV than the structure with D_{6H} and both structure has the $^1A_{1G}$ electronic symmetry for the $C_{10}H_2$@(6,0)-SWCNT system.

For the isolated $C_{10}H_2$ (polyyne), predicted electronic symmetry is $^1\Sigma_{1G}$ and has the $D_{\infty H}$ point group. As seen in Figure 18, the plotted electron density showed that while three of first five highest occupied molecular orbitals (HOMO/HOMO-3/HOMO-4 with the A_g, B_{1u} and A_{1u} symmetries, respectively) only belong to the (6,0)-SWCNT, the HOMO-1 and HOMO-2 with the B_{2u} and B_{3u} symmetry belong not only to both of the $C_{10}H_2$@(6,0)-SWCNT and but also there is a significant bonding interaction between the polyyne molecule ($C_{10}H_2$) and

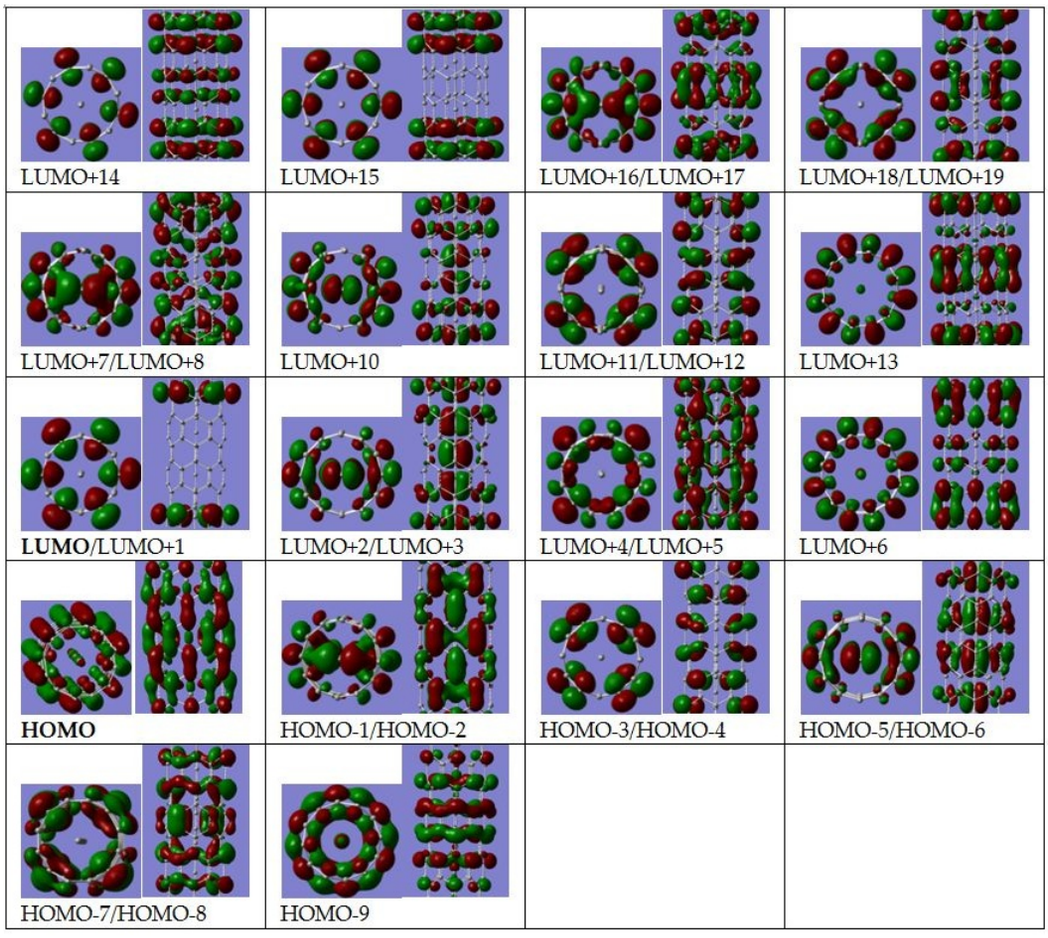

Figure 18. Calculated electron density of the molecular orbitals (MOs), HOMOs and LUMOs, of $C_{10}H_2$@(6,0)-SWCNT

(6,0)-SWCNT in the ground state. As seen in Table 6, the lowest unoccupied molecular orbital, LUMO (B_{3u})/LUMO + 1(B_{2g})/LUMO + 4 (A_g) LUMO + 5(B_{1g}) and LUMO + 6(B_{1u}) and lies about 0.43/0.43/0.89/0.89 and 1.66 eV above the HOMO (A_g) belong to the SWCNT only and the LUMO + 1(B_{3u})/LUMO + 2 (B_{2u}) belongs to the polyyne molecule and the SWCNT. However, the LUMO + 7(B_{3g})/LUMO + 8(B_{2g}) and LUMO + 9(B_{3g}) belong not only to both the $C_{10}H_2$@(6,0)-SWCNT (lies 1.99 /1.99 and 2.39 eV above the HOMO (A_g)), but there is a significant sigma bonding interaction in the excited states as seen in Figure 16.

The bonding interactions between $C_{10}H_2$ and (6,0)-SWCNT in the ground state leading to the increase the triple bond lengths and decrease the double C-C bond lengths within the polyyne molecule ($C_{10}H_2$) when encapsulated inside the (6,0)-SWCNT relative to its corresponding bond distance of the isolated single polyyne chain molecules ($C_{10}H_2$).

For instance, C-C bond distances in the encapsulated $C_{10}H_2$ molecules: 1.25974, 1.26769, 1.33655, 1.24771, 1.35216, 1.24771, 1.33655, 1.26769, 1.25974 Å and corresponding C-C bond distances in the isolated one: 1.22161, 1.35656, 1.23246, 1.34527, 1.23515, 1.34527, 1.23246, 1.35656, 1.22161 Å. These σ-bonding interactions between $C_{10}H_2$ and (6,0)-SWCNTs in the ground and excited states may be aspirant for the charge transfer between the molecule and

$C_{10}H_2$@(6,0)-SWCNTs			$C_{10}H_2$	
MOs	Sym.	ΔE(eV)	Sym.	ΔE(eV)
LUMO + 14	B_{3g}		$3.47SG_u$	13.87
LUMO + 13	A_g		$2.86PI_g$	13.24
LUMO + 12	B_{1u}		$2.72PI_g$	13.24
LUMO + 11	A_u		$2.72SG_g$	12.57
LUMO + 10	B_{2g}		$2.39SG_u$	11.56
LUMO + 9	B_{3g}		$2.39PI_u$	11.07
LUMO + 8	B_{2g}		$1.99PI_u$	11.07
LUMO + 7	B_{3g}		$1.99SG_g$	9.16
LUMO + 6	B_{1u}		$1.66SG_u$	9.15
LUMO + 5	B_{1g}		$0.89PI_g$	8.55
LUMO + 4	A_g		$0.89PI_g$	8.55
LUMO + 3	B_{2u}		$0.87PI_u$	6.11
LUMO + 2	B_{3u}		$0.87PI_u$	6.11
LUMO + 1	B_{2g}		$0.43PI_g$	3.90
LUMO	B_{3u}		$0.43PI_g$	3.90
HOMO	A_g		$-0.00PI_u$	0.00
HOMO-1	B_{2u}		$-0.19PI_u$	0.00
HOMO-2	B_{3u}		$-0.19PI_g$	-1.53
HOMO-3	B_{1u}		$-0.23PI_g$	-1.53
HOMO-4	A_u		$-0.23PI_u$	-2.86
HOMO-5	B_{3g}		$-1.55PI_u$	-2.86
HOMO-6	B_{2g}		$-1.55PI_g$	-3.87
HOMO-7	A_g		-1.91	

Table 6. Calculated energy levels ΔE(eV) of the molecular orbitals (MOs) for the $C_{10}H_2$@(6,0)-SWCNTs and $C_{10}H_2$ relative to their the highest molecular orbital (HOMO)

the SWCNT, which was observed between the polyyne and nanoparticles by the SERS as mentioned above.

The calculated vertical dipole allowed electronic transitions ($S_0 \rightarrow S_n$) of the $C_{10}H_2$@(6,0)-SWCNTs up to 0.52 eV are given in Table 7. Because of the technical difficulty, it was unable to calculate the higher electronic transitions that can provide more detailed information about internal conversion (IC) and inter system crossing (ISC). The lowest dipole allowed vertical electronic transitions $S_0(A_{1g}) \rightarrow S_7(B_{3u})$ as results of the HOMO-3→ LUMO + 1 and HOMO→ LUMO + 2 transitions and $S_0(A_{1g}) \rightarrow S_7(B_{2u})$ transition as a result of the HOMO-4->LUMO + 1 and HOMO→ LUMO + 3 transitions,the second lowest dipole allowed vertical

http://dx.doi.org/10.5772/51486

electronic transitions $S_0(A_{1g})\rightarrow S_{11}(B_{3u})$ due to the HOMO-3→ LUMO + 1 and HOMO→ LUMO + 2 transitions, and $S_0(A_{1g})\rightarrow S_{12}(B_{2u})$ transition because of the HOMO-4→ LUMO + 1 and HOMO→ LUMO + 3 transitions clearly indicate that the existence of charge transfer from the SWCNT to the polyyne molecules when examine the electron density of the HOMO and LUMOs involved in these transitions. When we examine the calculated vertical electronic transitions together with the calculated energy levels of molecular orbitals (MOs) of the encapsulated polyyne molecule inside the SWCNT, the IC and ISC can be expected.

Based on these calculations, the molecule encapsulated inside the nanotubes (NTs) can be used as energy conversion systems as a consequence of charge transfer between them. This illustration also can reflect on the intensity of the Raman bands at the resonance excitation energy where the charge transfer takes place between the molecules or particle and the nanotubes.

$S_0(A_{1G})\rightarrow S_n$						$S_0\rightarrow S_n$				
S_n	Sym.	H→L	CI	T_e(eV)	f	S_n	Sym.	H→L	CI	T_e(eV)
S_1	B_{2g}	H-"/>L+1	-0.84	0.06		S_{13}	B_{1g}	H-2-"/>L+3	-0.47	0.36
S_2	B_{3u}	H-"/>L	-0.83	0.06				H-1-"/>L+2	0.48	
S_3	B_{1g}	H-1-"/>L	0.61	0.08		S_{14}	A_g	H-2-"/>L+2	-0.49	0.37
S_4	A_g	H-2-"/>L	0.61	0.08				H-1-"/>L+3	0.49	
S_5	A_u	H-1-"/>L+1	0.62	0.09				H-"/>L+4	-0.15	
S_6	B_{1u}	H-2-"/>L+1	0.62	0.09		S_{15}	B_{1g}	H-2-"/>L+3	0.49	0.37
S_7	B_{3u}	H-3-"/>L+1	0.37	0.23	0.0001			H-1-"/>L+2	0.48	
		H-"/>L+2	0.56					H-"/>L+5	-0.15	
S_8	B_{2u}	H-4-"/>L+1	0.37	0.23	0.0001	S_{16}	A_g	H-2-"/>L+2	-0.13	0.41
		H-"/>L+3	0.57					H-1-"/>L+3	0.13	
S_9	B_{2g}	H-4-"/>L+3	-0.14	0.25				H-"/>L+4	0.60	
		H-3-"/>L	0.53			S_{17}	B_{1g}	H-2-"/>L+3	0.12	0.41
		H-3-"/>L+2	0.14					H-1-"/>L+2	0.12	
S_{10}	B_{3g}	H-4-"/>L	0.53	0.25				H-"/>L+5	0.60	
		H-4-"/>L+2	-0.14			S_{18}	B_{3g}	H-4-"/>L+2	-0.49	0.50
		H-3-"/>L+3	-0.14					H-3-"/>L+3	0.49	
S_{11}	B_{3u}	H-3-"/>L+1	0.40	0.30	0.0012	S_{19}	B_{2u}	H-2-"/>L+5	-0.51	0.51
		H-"/>L+2	-0.39					H-1-"/>L+4	0.52	
S_{12}	B_{2u}	H-4-"/>L+1	0.40	0.30	0.0012	S_{20}	A_u	H-4-"/>L+4	-0.44	0.52
		H-"/>L+3	-0.39					H-3-"/>L+5	0.44	

Table 7. The calculated vertical electronic transitions (Te; in eV) of $C_{10}H_2$@(6,0)-SWCNTs; S_0(A1g) → Sn. where the f and CI stand for the oscillator strength and the configurationally interaction coefficients, respectively. The Letters H and L stands for HOMO and LUMO, respectively.

Author details

Metin Aydin[1] and Daniel L. Akins

1 Department of Chemistry, Faculty of Art and Sciences, Ondokuz Mayıs University, Samsun, Turkey

Center for Analysis of Structures and Interfaces (CASI), Department of Chemistry, The City College of The City University of New York, New York, USA

References

[1] Iijima, S. (1991). *Nature.*, 354, 56.

[2] Dhriti, Nepal., Jung-Inn, Sohn., Wilhelm, K. Aicher, Seonghoon, Lee., & Kurt, E. Geckeler. (2005). *Biomacromolecules*, 6(6), 2919.

[3] Karajanagi, S. S., Yang, H., Asuri, P., Sellitto, E., Dordick, J. S., & Kane, R. S. (2006). *Langmuir*, 22, 1392.

[4] Hod, Finkelstein., Peter, M. Asbeck, & Sadik, Esener. (2003). *3rd IEEE Conference on Nanotechnology (IEEE-NANO)*, 1, 441.

[5] Zhou, C., Kong, J., Yenilmez, E., & Dai, H. (2000). *Science*, 290, 1552.

[6] Misewich, J. A., Martel, R., Avouris, P., Tsang, J. C., Heinze, S., & Tersoff, J. (2003). *Science*, 300, 783.

[7] Nitzan, A., & Ratner, R. A. (2003). *Science*, 300, 1384.

[8] Wen, D. S., & Ding, Y. L. (2004). *International Journal of Heat and Mass Transfer*, 47, 5181.

[9] Masuda, H., Ebata, A., Teramae, K., & Hishiunma, N. (1993). Netsu Bussei (Japan) , 4, 227.

[10] Carissa, S. Jones, Xuejun, Lu, Mike, Renn, Mike, Stroder, & Wu-Sheng, Shih. (2009). *Microelectronic Engineering*, DOI: j.mee.2009.05.034.

[11] Jung, S. M., Jung, H. Y., & Suh, J. S. (2009). Sensors and ActuatorsB. , 139, 425.

[12] Rueckes, T., Kim, K., Joselevich, E., Tseng, G. Y., Cheung, C. L., & Lieber, C. M. (2000). *Science*, 289, 94.

[13] Michael, J. O'Connell, Sergei, M. Bachilo, Chad, B. Huffman, Valerie, C. Moore, Michael, S. Strano, Erik, H. Haroz, Rialon, Kristy. L., Boul, Peter. J., Noon, William. H., Carter, Kittrell, Ma, Jianpeng., Robert, H. Hauge, Weisman, R. Bruce, & Smalley, E. Richard. (2002). *Science*, 297, 593.

[14] Bachilo, S. M., Strano, M. S., Kittrell, C., Hauge, R. H., Smalley, R. E., & Weisman, R. B. (2002). *Science*, 298, 2361.

[15] Hartschuh, A., Pedrosa, H. N., Novotny, L., & Krauss, T. D. (2003). *Science*, 301, 1354.

[16] Maultzsch, J., Pomraenke, R., Reich, S., Chang, E., Prezzi, D., Ruini, A., Molinari, E., Strano, M. S., Thomsen, C., & Lienau, C. (2006). *Phys. Stat. Sol. B*, 243(13), 3204.

[17] Chang, E., Bussi, G., Ruini, A., & Molinari, E. (2004). *Phys. Rev. Lett.*, 92, 196401.

[18] Spataru, C. D., Ismail-Beigi, S., Benedict, L. X., & Louie, S. G. (2004). *Phys. Rev. Lett.*, 92, 077402.

[19] Perebeinos, V., Tersoff, J., & Avouris, P. (2004). Phys. Rev. Lett. , 92, 257402.

[20] Won-Il, Park, Kim, Hun-Sik, Kwon, Soon-Min, Hong, Young-Ho, & Jin, Hyoung-Joon. (2009). *Carbohydrate Polymers*, 77, 457.

[21] Meng, Lingjie, Fu, Chuanlong, & Lu, Qinghua. (2009). *Natural Science*, 19, 801.

[22] Hsieh, C. T., & Lin, Y. T. (2006). Microporous Mesoporous Mater. , 93, 232.

[23] Davis, J. J., Coleman, K. S., Azamian, B. R., Bagshaw, C. B., & Green, M. L. H. (2003). Chem Eur J. , 9(16), 3732.

[24] Poenitzsch, V. Z., Winters, D. C., Xie, H., Dieckmann, G. R., Dalton, A. B., & Musselman, I. H. (2007). J Am ChemSoc, , 129(47), 14724.

[25] Carbon nanotube science:. (2009). *Synthesis, Properties and Applications, by P.J.F. Harris (Cambridge University Press, Cambridge).*

[26] Zunfeng, Liu, et al. (2010). *Journal of Nanoscience and Nanotechnology*, 10, 5570.

[27] Istvan, Robel, Bruce, A, & Kamat, Prashant V. (2005). *Advanced Materials*, 17(20), 2458.

[28] Olek, M., Busgen, T., Hilgendorff, M., & Giersig, M. (2006). *Journal of Physical Chemistry B*, 110(26), 12901.

[29] Kazuhiro, Yanagi, Konstantin Iakoubovskii, Hiroyuki Matsui, Hiroyuki, Matsuzaki, Hiroshi, Okamoto, Yasumitsu, Miyata, Yutaka, Maniwa, Said, Kazaoui, Nobutsugu, Minami, & Hiromichi, Kataura. (2007). *J. Am. Chem. Soc.*, 129(16), 4992.

[30] Yuika, Saito, Kazuhiro, Yanagi, Norihiko, Hayazawa, Hidekazu, Ishitobi, Atsushi, Ono, Hiromichi, Kataura, & Satoshi, Kawata. (2006). *Jap. J. Appl. Phys.*, 45(12), 9286.

[31] Alvarez, L., Almadori, Y., Arenal, R., Babaa, R., Michel, T., Le Parc, R., Bantignies, J. -L, Jousselme, B. , Palacin, S. , Hermet, P., & Sauvajol, J. L. (2011). J. Phys. Chem. C, , 115(24), 11898.

[32] Srinivasan, C. (2008). *Current Science*, 94, 300.

[33] Hilder, T. A., & Hill, J. M. (2008). Current Applied Physics , 8, 258.

[34] Clendenin, J., Kim, J., & Tung, S. (2007). *Proc of 2007 2nd IEEE conference on Nanotechnology*, 1028.

[35] Bianco, A., Kostarelos, K., & Prato, M. (2005). *Current Opinion in Biotechnology*, 9, 674.

[36] Nasreen, G., Chopra, R. J., Luyken, K., Cherrey, Vincent. H., Crespi, Marvin. L., Cohen, Steven. G. Louie, & Zettl, A. (1995). Science. , 269, 966.

[37] Golberg, D., Bando, Y., Han, W., Kurashima, K., & Sato, T. (1999). *Chem. Phys. Lett.*, 308, 337.

[38] Tang, C. C., Bando, Y., Sato, T., & Kurashima, K. (2002). Chem. Commun. , 121, 290.

[39] Dresselhaus, M. S., Dresselhaus, G., & Eklund, P. C. (1996). Science of Fullerenes and Carbon Nanotubes. Academic Press, San Diego, CA.

[40] Rubio, A., Corkill, J., & Cohen, M. L. (1994). Phys. Rev. B. , 49, 5081.

[41] Zhang, D., & Zhang, R. Q. (2003). Chem. Phys. Lett. , 371, 426.

[42] Mirzaei, M., & Hadipour, N. L. (2008). Physica E, , 40, 800.

[43] Park, C. H., Spataru, C. D., & Louie, S. G. (2006). *Physical Review Letters*, 96, 126105.

[44] Wirtz, L., Marini, A., & Rubio, A. (2006). *Physical Review Letters*, 96, 126104.

[45] Chunyi, Zhi, Yoshio, Bando, Chengchun, Tang, & Dmitri, Golberg. (2010). *Materials Science and Engineering R*, 70, 92.

[46] Kam, N. W. S., O'Connell, M., Wisdom, J. A., & Dai, H. (2005). *PNAS*, 102, 11600.

[47] Gaussian, Inc. *Carnegie Office Park-Bulding 6, Pittsburgh, PA106, USA.*

[48] (a) C. Guo, M. Aydin, H. R. Zhu, D. L. Akins, J. Phys. Chem. B 106 (2002) 5447; (b) H, Guo, X. Zhang, M. Aydin, W. Xu, H. R. Zhu, D. L Akins, Journal of Molecular Structure 689 (2004) 153; (c) M. Aydin, F. Jean-Mary, N. Stevens, D. L. Akins, J. Phys. Chem. B 108(2004) 9695; (d) W. Xu, M. Aydin, S. Zakia, D. L. Akins, J. Phys. Chem. B 108 (2004) 5588; (e) M. Aydin, J. R. Lombardi, J. Phys. Chem. A. 113 (2009) 2809; (f) M. Aydin, D.L. Akins, Vibrational Spectroscopy 53 (2010) 163; (g) M. Aydin, Vib. Spectrosc. 66 (2013) 30, (h) Metin Aydin and Daniel Akins (2011), Geometric and Spectroscopic Properties of Carbon Nanotubes and Boron Nitride Nanotubes, Electronic Properties of Carbon Nanotubes, Prof. Jose Mauricio Marulanda (Ed.), ISBN: 978-953-307-499-3, InTech, Available from: http://www.intechopen.com/books/electronic-properties-of-carbon-nanotubes/geometric-and-spectroscopic-properties-of-carbon-nanotubes-and-boron-nitride-nanotubes; (i) Metin AYDIN Photofragmentation Spectroscopy, Publisher: VDM Verlag, 2009; ISBN: 3639152891.

[49] Pfeiffer, R., Simon, F., Kuzmany, H., & Popov, V. N. (2005). *Phys. Rev.*, B72, 161404(R).

[50] Lee, Eun-Ju, Yoon, Jin-San, Kim, Mal-Nam, & Park, Eun-Soo. (1970). Preparation and Applicability of Vinyl Alcohol Group Containing Polymer/MWNT Nanocomposite

Using a Simple Saponification Method. *Carbon Nanotubes- Polymer Nanocomposites, Siva Yellampalli (Ed.)*, 978-9-53307-498-6, InTech, Available from:, http://www.intechopen.com/books/carbon-nanotubes-polymer-nanocomposites/preparation-and-applicability-of-vinyl-alcohol-group-containing-polymer-mwnt-nanocomposite-using-a-s.

[51] Milani, A., Lucotti, A., Russo, V., Tommasini, M., Cataldo, F., Li Bassi, A., & Casari, C. S. (2011). *J. Phys. Chem. C*, 115, 12836.

[52] Ravagnan, L., Siviero, F., Lenardi, C., Piseri, P., Barborini, E., Milani, P., Casari, C. S., Li Bassi, A., & Bottani, C. E. (2002). Phys. Rev. Lett. 89285506

[53] Casari, C. S., Li Bassi, A., Ravagnan, L., Siviero, F., Lenardi, C., Piseri, P., Bongiorno, G., Bottani, C. E., & Milani, P. (2004). *Phys. Rev. B*, 69075422.

[54] Daisuke, Nishide, Hirofumi, Dohi, Tomonari, Wakabayashi, Eiji, Nishibori, Shinobu, Aoyagi, Masashi, Ishida, Satoshi, Kikuchi, Ryo, Kitaura, Toshiki, Sugai, Makoto, Sakata, & Hisanori, Shinohara. (2006). *Chem. Phys. Letter*, 428, 356.

[55] Nishide, D., Dohi, H., Wakabayashi, T., Nishibori, E., Aoyagi, S., Ishida, M., Kikuchi, S., Kitaura, R., Sugai, T., Sakata, M., & Shinohara, H. (2006). Chem. Phys. Lett. , 428, 356.

[56] Malard, L. M., Nishide, D., Dias, L. G., Rodrigo, B. Capaz, Gomes, A. P., Jorio, A., Achete, C. A., Saito, R., Achiba, Y., Shinohara, H., & Pimenta, M. A. (2007). *Phys. Rev. B*, 76, 233412.

[57] Tabata, H, Fujii, M, Hayashi, S, Doi, T, & Wakabayashi, T. (2006). *Carbon*, 44, 3168, WakabayashiTTabataHDoiTNagayamaHOkudaKUmedaRHisakiISonodaMTobeY-MinematsuTHashimotoKHayashiS, 2007, *Chem. Phys. Lett*., 433, 296.

[58] Pino, T, Ding, H, Güthe, F, & Maier, J. P. (2001). *J. Chem. Phys*., 114, 2208.

[59] Cumings, A. Zettl, Chem. Phys. Lett. 316 (2000) 211.

[60] N. R. Arutyunyan, E. D. Obraztsova, M. Silly, P. Jaffrennou, B. A. Tretout, A. Loiseau, A. L. Chuvilin, Phys. Stat. Sol. (b) 243(13) (2006) 3316.

[61] S. Y. Bae, H. W. Seo, J. Park, Y. S. Choi, J. C. Park, S. Y. Lee, Chem. Phys. Lett. 374 (2003) 534.

[62] W.-Q. Han, H.-G. Yu, C. Zhi, J. Wang, Z. Liu,T. Sekiguchi, Y. Bando, Nano Lett. 8(2) (2008) 491.

[63] E. A. Obraztsova, D. V. Shtansky, A. N. Sheveyko, M. Yamaguchi, A. M. Kovalskii, D. Golberg, Scripta Mater. 67 (2012) 507.

[64] C. H. Lee, J. Wang, V. K. Kayatsha, J. Y. Huang, Y. K. Yap, Nanotechnology 19 (2008) 455605.

IntechOpen